STUDY OF PROTON INTERACTIONS IN THE DSTAU(NA65) EXPERIMENT AT THE CERN-SPS

A THESIS SUBMITTED TO
THE GRADUATE SCHOOL OF NATURAL AND APPLIED SCIENCES
OF
MIDDLE EAST TECHNICAL UNIVERSITY

BY

EMIN YÜKSEL

IN PARTIAL FULFILLMENT OF THE REQUIREMENTS
FOR
THE DEGREE OF MASTER OF SCIENCE
IN
PHYSICS

SEPTEMBER 2024

Approval of the thesis:

STUDY OF PROTON INTERACTIONS IN THE DSTAU(NA65) EXPERIMENT AT THE CERN-SPS

submitted by **EMIN YÜKSEL** in partial fulfillment of the requirements for the degree of **Master of Science in Physics Department, Middle East Technical University** by,

Prof. Dr. Naci Emre Altun
Dean, Graduate School of **Natural and Applied Sciences** _____

Prof. Dr. Seçkin Kürkcüoğlu
Head of Department, **Physics** _____

Prof. Dr. Ali Murat Güler
Supervisor, **Physics, METU** _____

Examining Committee Members:

Prof. Dr. İsmail Turan
Physics, METU _____

Prof. Dr. Ali Murat Güler
Physics, METU _____

Assoc. Prof. Dr. Aysuhan Ozansoy
Physics, Ankara University _____

Date:03.09.2024

I hereby declare that all information in this document has been obtained and presented in accordance with academic rules and ethical conduct. I also declare that, as required by these rules and conduct, I have fully cited and referenced all material and results that are not original to this work.

Name, Surname: Emin Yüksel

Signature :

ABSTRACT

STUDY OF PROTON INTERACTIONS IN THE DSTAU(NA65) EXPERIMENT AT THE CERN-SPS

Yüksel, Emin
M.S., Department of Physics
Supervisor: Prof. Dr. Ali Murat Güler

September 2024, 77 pages

The Standard Model consists of three generations of leptons, with the neutrinos corresponding to each generation being extensively studied and well understood, except for the tau neutrino (ν_τ). While the interaction of the ν_τ has been observed and its cross section measured in a few experiments, the number of observed interactions remains limited and is accompanied by significant uncertainties. The DsTau (NA65) experiment at CERN-SPS aims to measure the cross-section of D_s meson production, which will provide a precise understanding of the ν_τ production. The DsTau experiment employs a nuclear emulsion-based detector with a sub-micron spatial resolution to capture the small kink in the $D_s \to \tau$ decay topology. In this thesis, we present the first results of the data analysis of the 2018 run. A new method is developed for the proton track reconstruction through the full detector. The proton interaction vertex is analyzed in detail, and data are compared with different Monte Carlo event generator predictions. The findings presented in this study can be utilized to improve the predictions of event generators.

Keywords: DsTau experiment, Proton interactions, KNO-G scaling

ÖZ

CERN-SPS'DEKİ DSTAU(NA65) DENEYİNDE PROTON ETKİLEŞİMLERİNİN İNCELENMESİ

Yüksel, Emin
Yüksek Lisans, Fizik Bölümü
Tez Yöneticisi: Prof. Dr. Ali Murat Güler

Eylül 2024 , 77 sayfa

Standart Model, her biri için nötrinoların kapsamlı bir şekilde incelendiği ve iyi anlaşıldığı üç nesil leptondan oluşur, tau nötrinosu (ν_τ) hariç. ν_τ etkileşimi gözlemlenmiş ve bir kaç deneyde tesir kesiti ölçülmüş olsa da, gözlemlenen etkileşimlerin sayısı sınırlı kalmakta ve önemli belirsizliklerle birlikte gelmektedir. CERN-SPS'deki DsTau (NA65) deneyi, D_s mezon üretim tesir kesitini ölçmeyi amaçlamaktadır, bu da ν_τ üretiminin kesin bir şekilde anlaşılmasını sağlayacaktır. DsTau deneyi, $D_s \rightarrow \tau$ bozunma topolojisindeki küçük kırılımı yakalamak için mikron altı uzaysal çözünürlüğe sahip nükleer emülsiyon tabanlı bir dedektör kullanır. Bu tezde, 2018 çalışmasının veri analizinin ilk sonuçlarını sunuyoruz. Tüm dedektör boyunca proton izi rekonstrüksiyonu için yeni bir yöntem geliştirilmiştir. Proton etkileşim noktası detaylı bir şekilde analiz edilmiş ve veriler farklı Monte Carlo olay üreteçlerinin sonuçları ile karşılaştırılmıştır. Bu çalışmada sunulan bulgular, olay üreteçlerinin tahminlerinin iyileştirilmesi için kullanılabilir.

Anahtar Kelimeler: DsTau deneyi, Proton etkileşimleri, KNO-G ölçeklendirmesi

To my family

ACKNOWLEDGMENTS

I gratefully acknowledge TENMAK for supporting our project, "Setup and testing of new emulsion-based experiments and physics research beyond the standard model at CERN" (Grant no. 2022TENMAK(CERN)-A5.H3.F2-1). My sincere thanks go to all members of the DsTau collaboration, with special mention to Osamu Sato and Akitaka Ariga for their invaluable assistance and knowledge sharing, which were crucial to the success of this study. I am also deeply grateful to my friends from the METU DsTau team, Canay Öz, and especially to my beloved Neşe Ergin, for their support throughout my research. Additionally, I wish to express my appreciation to my dear friends Fatih Ünal, Mehmet Bilgiç, Ahmet Furkan Yıldırım, and Emirhan Kurtuluş for their patience and encouragement over the years. Special thanks to my brothers, Kenan and Halil, and my precious parents, Hacer and Ali, for their constant patience and support during my academic journey. Lastly, I am profoundly thankful to Prof. Dr. Ali Murat Güler, who supervised this thesis and generously shared his expertise, knowledge, and wisdom with me.

TABLE OF CONTENTS

ABSTRACT v

ÖZ vii

ACKNOWLEDGMENTS x

TABLE OF CONTENTS xi

LIST OF TABLES xiv

LIST OF FIGURES xv

LIST OF ABBREVIATIONS xx

CHAPTERS

1 INTRODUCTION 1

2 PHENOMENOLOGY OF STANDARD MODEL AND TAU NEUTRINO PRODUCTION 5

2.1 Standard Model 5

2.1.1 Fundamental Forces 6

2.1.2 Leptons 7

2.1.3 Quarks 7

2.1.4 Hadrons 9

2.1.4.1 Mesons 10

2.1.4.2 Baryons 12

2.2 Charm hadroproduction 13
2.3 D_s Meson Decay 15
2.3.1 Pure Leptonic Decays 16
2.3.2 Semi-leptonic Decays 17
2.3.3 Pure Hadronic Decays 18
3 THE DSTAU EXPERIMENT 19
3.1 Motivation of the Experiment 19
3.2 Experimental Setup 20
3.3 Nuclear Emulsion Films 22
3.4 Target Mover 23
3.5 Emulsion Scanning 24
4 DATA RECONSTRUCTION AND ANALYSIS 27
4.1 Reconstruction 27
4.1.1 Base-track reconstruction 29
4.1.2 Fine alignment 29
4.1.3 Volume-track reconstruction 30
4.1.4 Proton Linking 31
4.1.4.1 Proton Selection 31
4.1.4.2 Track Linking 33
4.1.4.3 Segment Linking 37
4.1.4.4 Workflow 38
4.1.5 Vertexing 40
4.1.6 Data conversion to ROOT format 40

4.1.7 Data Quality Check . . . 42
4.2 Monte Carlo Simulation . . . 45
4.3 Efficiency Estimation . . . 45
4.3.1 Selection of Minimum Ionizing Particles . . . 46
4.3.2 Vertex Reconstruction Efficiency (ε_{vtx}) . . . 49
4.3.3 Proton Linking Efficiency (ε_{plink}) . . . 50
4.3.4 Matching Efficiency (ε_{match}) . . . 51
4.3.5 Acceptance Efficiency (ε_{acc}) . . . 52
4.3.6 Total Efficiency (ε_{tot}) . . . 53
4.3.7 Data-Driven Efficiencies . . . 54
4.3.8 Proton Purity . . . 57
4.3.9 Multiplicity Dependence of Vertex Reconstruction Efficiency . 57
5 FIRST RESULTS FROM PILOT RUN . . . 59
5.1 Proton Interaction Rate . . . 59
5.2 MC / Data Comparisons . . . 60
5.3 KNO-G Scaling . . . 68
5.3.1 Formulation of KNO-G Scaling . . . 68
5.3.2 Application of KNO-G Scaling to DsTau Multiplicity Distribution . . . 70
6 CONCLUSIONS . . . 73
REFERENCES . . . 75

LIST OF TABLES

TABLES

Table 2.1 Additive quantum numbers of the quarks. 9

Table 4.1 Vertex reconstruction efficiency for each tungsten plate. 49

Table 4.2 Proton linking efficiency for each tungsten plate. 50

Table 4.3 Matching efficiency for each tungsten plate. 51

Table 4.4 Vertex reconstruction efficiency for each tungsten plate with acceptance cut. 53

Table 4.5 Total efficiency for each tungsten plate. 54

Table 4.6 Table of estimated data-driven efficiency through track density using linear functions. 56

Table 5.1 The proton interaction rate per unit length in the tungsten is estimated for data and EPOS. 60

Table 5.2 Obtained KNO-G fit parameters 70

LIST OF FIGURES

FIGURES

Figure 1.1 The location of the North Area. 2

Figure 2.1 The Standard Model of elementary particles. 6

Figure 2.2 Bound states of hadrons. 10

Figure 2.3 SU(3) weigth diagram for light mesons forming a nonet. 11

Figure 2.4 SU(4) weigth diagram for light mesons forming a 16-plet. 12

Figure 2.5 SU(4) weigth diagrams for baryons [7]. Symmetric 20-plet (left), mixed-symmetric 20-plet (right). 13

Figure 2.6 Feynman diagrams of the QCD fusion process. (a) $q\bar{q}$ s-channel process, (b) gg s-channel process, (c) gg t-channel process, and (d) gg u-channel process. 14

Figure 2.7 D_s^+ branching fractions. 15

Figure 2.8 $D_s^+ \to \tau\nu_\tau$ decay. 16

Figure 2.9 $D_s^+ \to \phi^0 e\nu_e$ decay. 17

Figure 2.10 $D_s^+ \to K^+K^0$ decay. 18

Figure 3.1 Cross section of three neutrino flavors. The Standard Model prediction is indicated as dashed line. 19

Figure 3.2 Double kink topology of $D_s \to \tau \to \nu_\tau$. 20

Figure 3.3 Schematic view of test run DsTau detector. 21

Figure 3.4 Previous detector configuration used during the test run with a lead target ECC (top). Current detector configuration in use with a tungsten target ECC (bottom). 22

Figure 3.5 Left: Composite structure of an emulsion plate. Middle: Silver halide crystals embedded within the nuclear emulsion. Right: Microscopic image of a particle track. 23

Figure 3.6 Schematics of the target mover. 24

Figure 3.7 A photograph of the Hyper Track Selector. 24

Figure 3.8 A schematics of automated nuclear emulsion scanning system. . 25

Figure 4.1 Representation of sub-areas and sub-volumes. 27

Figure 4.2 Flowchart of DsTau reconstruction. 28

Figure 4.3 Base-track reconstruction process. 29

Figure 4.4 (a) Two tracks converging in a high-density environment. (b) Visualization of the calculation of a^{pos} and a^{angle}. 30

Figure 4.5 The distribution of proton track angles in the XZ and YZ planes is presented, and a Gaussian fit is applied. The region within 3-sigma is considered the primary proton track. 32

Figure 4.6 Visualization of the proton linking method. The upper section displays the first sub-volume, while the lower section presents the second sub-volume. 33

Figure 4.7 3D representation of sub-zones with transition area. 34

Figure 4.8 Sequential stages of the proton linking process. Double-headed arrows indicate parallel processes, while single-headed arrows denote sequential processes and their directions. 35

Figure 4.9 An illustration of tracks transitioning to an adjacent sub-area. . . 36

Figure 4.10 A lateral cross-section of the sub-volume is illustrated. Dashed lines indicate the sub-zones and the colored regions aligned with the beam axis represent the sub-zones after extrapolation. 37

Figure 4.11 Proton linking flowchart. 39

Figure 4.12 A subset of the data containing fully reconstructed proton interactions is visualized using the FEDRA [28]. The visualization shows linked primary proton tracks, associated vertices, and daughter particles. For clarity, only a few of the tracks are selected and displayed. . . 41

Figure 4.13 Comparison of the spatial distribution of vertices along the transverse axis: the left panel displays module PD05, while the right panel shows module PD06. 42

Figure 4.14 Spatial distribution of vertices that do not match with proton links in transverse axis. Dense areas below 40000 indicates low efficiency sub-areas. 43

Figure 4.15 Data quality histograms for high-quality sub-area (left), and low-quality sub-area (right). 43

Figure 4.16 Selected 21 high-quality sub-areas is depicted in green. 44

Figure 4.17 Distance between true and reconstructed vertex position in X, Y, and Z axes. 46

Figure 4.18 Bethe-Bloch curve for μ in copper medium. 47

Figure 4.19 $\beta * Momentum$ histograms full view (left), zoomed (right) into 0-0.50 GeV/c region. 47

Figure 4.20 Multiplicity comparison between reconstructed and true MC before (left), and after $\beta * Momentum$ > 0.30 GeV/c cut (right). 48

Figure 4.21 $\beta * Momentum$ < 0.30 GeV/c vs PDGID distribution. 48

Figure 4.22 The z-axis distribution of vertex positions within the tungsten plate, including an acceptance cut of 18 microns, is shown. 52

Figure 4.23 The distribution of track density for both Monte Carlo simulations and experimental data is illustrated, with dots indicating the data and solid line is representing the EPOS result. 54

Figure 4.24 A scatter plot illustrating the relationship between MC efficiencies and track density is presented, along with a linear fit. The plots include efficiencies for vertex reconstruction, proton linkage, and total efficiency. 55

Figure 4.25 The efficiency of vertex reconstruction is analyzed as a function of the multiplicity of charged tracks at the vertex. 57

Figure 5.1 A comparison between MC simulations and experimental data for impact parameter is shown, MC is normalized to the number of tracks in the data. The lower section of the histogram illustrates the ratio of MC to data. The constant black line represents the data. 61

Figure 5.2 A comparison between MC simulations and experimental data for track multiplicity is shown, MC is normalized to the number of events in the data. The lower section of the histogram illustrates the ratio of MC to data. The constant black line represents the data. 62

Figure 5.3 A comparison between MC simulations and experimental data for track angle is shown, MC is normalized to the number of tracks in the data. The lower section of the histogram illustrates the ratio of MC to data. The constant black line represents the data. 63

Figure 5.4 The left panel displays the distribution of track slope versus multiplicity in the experimental data, EPOS and QGSJET respectively (from top to bottom). The right panel presents the same distribution but they are normalized to each multiplicity bin. 65

Figure 5.5 A comparison between MC simulations and experimental data for track slope less than 10 is shown, MC is normalized to the number of tracks in the data. The lower section of the histogram illustrates the ratio of MC to data. The constant black line represents the data. 66

Figure 5.6 A comparison between MC simulations and experimental data for track slope greater than or equal to 10 is shown, MC is normalized to the number of tracks in the data. The lower section of the histogram illustrates the ratio of MC to data. The constant black line represents the data. 67

Figure 5.7 (a) Multiplicity distribution with different center-of-mass energies. (b) Multiplicity axis normalized is normalized with mean multiplicity. (c) Probability axis is scaled with mean multiplicity so they coincide at each point. 68

Figure 5.8 Discrete multiplicity distribution at low energies. 70

Figure 5.9 KNO-G scaling fit on DsTau multiplicity distribution. 71

LIST OF ABBREVIATIONS

DONuT	Direct Observation of Nu-Tau
DsTau	The DsTau (NA65) Collaboration
OPERA	The Oscillation Project with Emulsion-tRacking Apparatus
MINOS	The Main Injector Neutrino Oscillation Search
T2K	Tokai to Kamioka
METU	Middle East Technical University
CERN	The European Organization for Nuclear Research
SM	Standard Model
QCD	Quantum ChromoDynamics
MIP	Minimum Ionizing Particle
MC	Monte Carlo
GEANT4	GEometry ANd Tracking
EPOS	Energy conserving quantum mechanical approach, based on Partons, parton ladders, strings, Off-shell remnants, and Splitting of parton ladders
ECC	Emulsion Cloud Chamber
MCS	Multiple Coulomb Scattering
SPS	Super Proton Synchrotron
HTS	Hyper Track Selector
3D	3 Dimensional

CHAPTER 1

INTRODUCTION

The Standard Model (SM) of particle physics offers a robust framework for understanding fundamental particles and their interactions. The concept of the SM was initially developed in the 1960s and has since been validated through numerous experiments. The SM has been highly successful, accurately predicting many phenomena and being confirmed by numerous experiments, including the discovery of the Higgs boson. However, it has limitations and is not a complete theory of fundamental interactions, as it does not encompass gravity, dark matter, dark energy, or the masses of neutrinos observed in oscillations.

Ongoing research aims to understand its drawbacks and pursue a more comprehensive theory of fundamental forces and particles. Consequently, particle physics seeks to develop broader and more robust theories, often referred to as "New Physics".

Lepton universality is a fundamental concept in the Standard Model of particle physics. It asserts that all leptons, including electrons (e), muons (μ), and taus (τ), interact with the weak force identically. The only difference between different lepton flavors is their masses. Therefore, any violation of lepton universality suggests the existence of a new physics beyond the Standard Model.

The DsTau experiment aims to measure the differential production cross-section of the D_s meson in proton-nucleus interactions at 400 GeV. A more precise understanding of D_s meson decays would reduce the uncertainty in tau-neutrino cross-section measurements. This would aid in testing Lepton Universality, a fundamental principle of the Standard Model. Additionally, these measurements can provide essential data for future neutrino-based experiments such as FASER, SND@LHC, and SHiP.

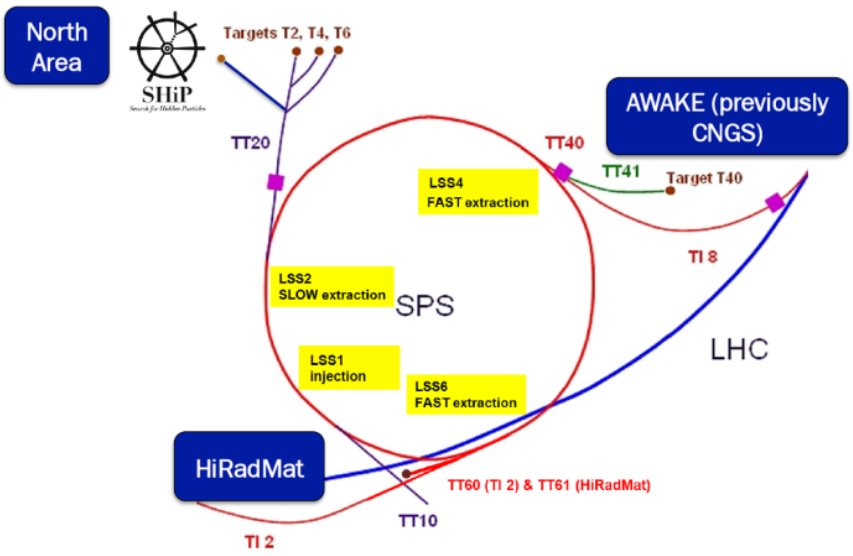


Figure 1.1: The location of the North Area.

The DsTau/NA65 experiment is conducted at CERN's Super Proton Synchrotron (SPS) in North Area 1.1. The SPS delivers proton beams with an energy of 400 GeV and an intensity of 4×10^{13} protons. Each proton spill has a duration of 1.2 seconds, followed by a cooldown interval of 7.2 seconds.

The primary objective of the DsTau experiment is to select and analyze the decay topology of D_s mesons into τ leptons and subsequent particles. The decay topology involves a double kink: the D_s meson decays into a τ lepton and a ν_τ, and the resulting τ lepton further decays into another ν_τ. D_s to τ decay is characterized by a minuscule kink angle, necessitating a detector with a sub-micron spatial resolution to study this process accurately. Nuclear emulsion films are used to measure such a tiny angle and are expected to have 4.9×10^9 protons on the target, with 2.3×10^8 protons expected to interact with the target. Only a subsample of the data from the 2018 pilot run has been analyzed, and this paper will present the results of that analysis.

Content of the thesis is as follows:

- **Chapter 2**: A brief explanation of elementary particles and lepton universality is given.
- **Chapter 3**: The DsTau experimental setup and analysis of nuclear emulsion are explained in detail.
- **Chapter 4**: The reconstruction of the DsTau data, along with the Monte Carlo generation and the efficiency estimation of the reconstruction process, is discussed here.
- **Chapter 5**: The first results of the DsTau experiment are presented.
- **Chapter 6**: Conclusion and summary are given.

CHAPTER 2

PHENOMENOLOGY OF STANDARD MODEL AND TAU NEUTRINO PRODUCTION

2.1 Standard Model

The Standard Model (SM) of particle physics stands as one of modern science's most successful theoretical frameworks, providing a comprehensive description of the fundamental particles and their interactions. The SM categorizes all known elementary particles into two groups: fermions, which constitute matter, and bosons, which mediate the fundamental forces [2].

Particles with non-integer spin numbers are called fermions, which obey the Pauli exclusion principle. Fermions are categorized into leptons and quarks, each having corresponding antiparticles. Leptons also include neutral particles known as neutrinos. Fermions constitute the fundamental building blocks of matter, with matter being composed of quarks and leptons. Conversely, particles with integer spin numbers are known as bosons and follow Bose-Einstein statistics. Bosons serve as force carriers. 2.1

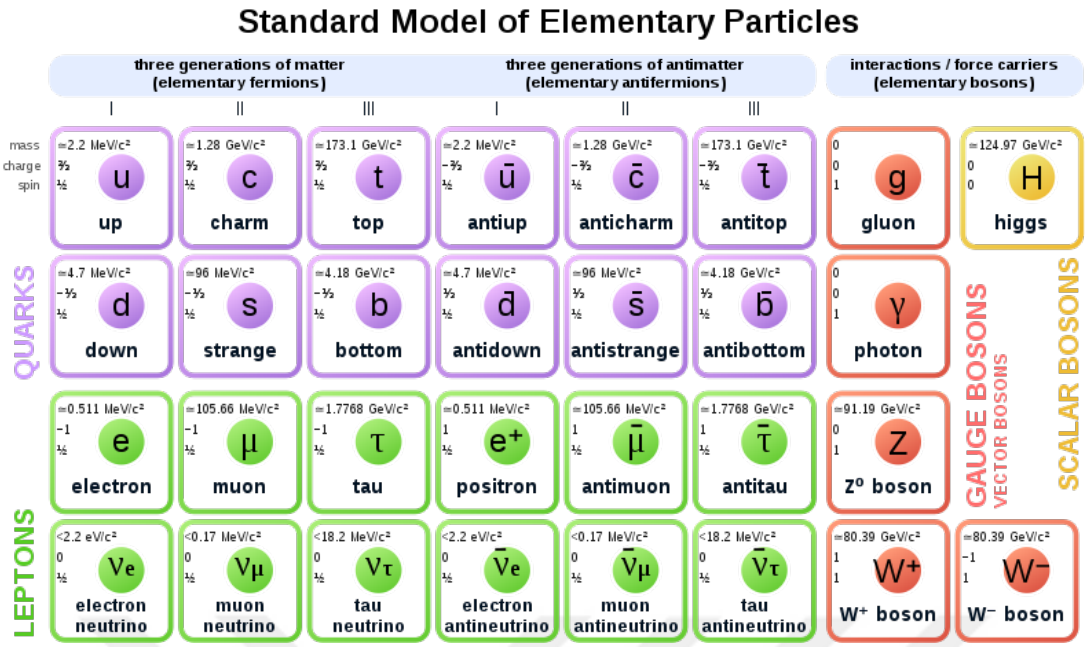


Figure 2.1: The Standard Model of elementary particles.

2.1.1 Fundamental Forces

The matter in the known universe consists of fermions that interact through fields, and each field is associated with a boson. These interactions through the field are also known as fundamental forces. Four different fundamental forces exist: Gravitational force, electromagnetic force, weak force, and strong force. The gravitational force is the most extended range yet most insignificant force. As we go through the strong force, the interaction range gets shorter, but the strength of the force increases.

Gravitation: The origin of the gravitational force is mass, and graviton mediates it. Although gravitational force has an infinite range, it is the weakest of the fundamental forces.

Weak: Weak interactions are the second weakest among the fundamental forces and are mediated by Z^0 and $W^{\pm}$ bosons, acting over a shorter range than electromagnetic interactions. Both quarks and leptons can participate in weak interactions. When mediated by $W^{\pm}$ bosons, these interactions are known as charge-current interactions and cause a change in the charge of the interacting particles. Unlike other funda-

mental forces, weak interactions do not conserve the charm and strangeness quantum numbers.

Electromagnetic: The electromagnetic force, the second strongest of the fundamental forces, is mediated by photons. This force originates from electric charge, allowing all charged particles to participate in electromagnetic interactions.

Strong: The strongest of all fundamental forces is the strong interaction. Strong interactions are mediated by gluons, which carry color charge and are exclusive to quarks. Quarks come in three distinct colors: red, green, and blue, while anti-quarks have corresponding anti-colors: anti-red, anti-green, and anti-blue. The total color charge must always be color-neutral in any composite quark system. The strength of the strong interaction increases as the distance between quarks increases and decreases as quarks come closer together. This phenomenon is known as asymptotic freedom [3].

2.1.2 Leptons

Leptons are categorized into three generations, each comprising a charged lepton and its neutrino. The first generation includes the electron (e), the second includes the muon (μ), and the third includes the tau (τ) particle. Leptons possess a negative electric charge and ½ spin, while their corresponding antiparticles have a positive charge. Neutrinos, associated with each lepton, are electrically neutral. Leptons do not have any color charge and, as a result, do not interact with the strong force.

2.1.3 Quarks

Quarks, like leptons, exist in three generations, with each generation containing two distinct flavors of quarks:

- First generation: Up and down quarks
- Second generation: Charm and strange quarks
- Third generation: Top and bottom quarks

Quarks possess non-integer electric charges and, similar to leptons, have corresponding antiparticles with opposite charges and a spin of ½. Quarks can interact with all four fundamental forces. In these interactions, the number of quarks is conserved, although the flavor of the quarks can change. Quarks have never been observed in isolation and are always confined in composite states.

Quarks are described by set of quantum numbers that characterized their properties [9]. These are:

- **Electric Charge:** Quarks possess fractional electric charges. Specifically, down, strange, and bottom quarks carry a charge of $-\frac{1}{3}$, whereas up, charm and top quarks have a charge of $+\frac{2}{3}$. Electric charge is conserved by strong and electromagnetic interactions.

- **Isospin:** The strong force is independent of electric charge, and protons and neutrons, having similar masses, experience the same strong force within the nucleus. Therefore, a new quantum number, known as isospin, is introduced to distinguish them. The down quark has an isospin component I_3 of $-\frac{1}{2}$, while the up quark has an I_3 of $+\frac{1}{2}$. Isospin is conserved by strong interactions.

- **Strangeness:** The strangeness quantum number represents the presence of strange quarks. Strange quarks are assigned a strangeness of -1. Strangeness is conserved in strong and electromagnetic interactions.

- **Charmness:** The charm quantum number represents the presence of charm quarks. Charm quarks have a charmness of +1. Charmness is conserved in strong and electromagnetic interactions.

- **Bottomness:** The bottomness quantum number represents the presence of bottom quarks. Bottom quarks are assigned a bottomness of -1. Bottomness is conserved in strong and electromagnetic interactions.

- **Topness:** The topness quantum number represents the presence of top quarks. Top quarks have a topness value of +1. Topness is conserved in strong and electromagnetic interactions.

- **Baryon Number:** Quarks possess a fractional baryon number of $\frac{1}{3}$, whereas

anti-quarks have a baryon number of $-\frac{1}{3}$. The baryon number is conserved in any interaction.

Additive quantum numbers of quarks are presented in Table 2.1.3.

Table 2.1: Additive quantum numbers of the quarks.

	d	**u**	**s**	**c**	**b**	**t**
Q - Electric Charge	$-\frac{1}{3}$	$+\frac{2}{3}$	$-\frac{1}{3}$	$+\frac{2}{3}$	$-\frac{1}{3}$	$+\frac{2}{3}$
I - Isospin	$\frac{1}{2}$	$\frac{1}{2}$	0	0	0	0
I_3 - Isospin Z-Component	$-\frac{1}{2}$	$+\frac{1}{2}$	0	0	0	0
S - Strangeness	0	0	-1	0	0	0
C - Charmness	0	0	0	$+1$	0	0
B - Bottomness	0	0	0	0	-1	0
T - Topness	0	0	0	0	0	$+1$
$\mathcal{B}$ - Baryon Number	$\frac{1}{3}$	$\frac{1}{3}$	$\frac{1}{3}$	$\frac{1}{3}$	$\frac{1}{3}$	$\frac{1}{3}$

These given quantum numbers are related to electric charge (Q) and this relation is formulated by Gell-Mann-Nishijima formula

$$Q = I_3 + \frac{\mathcal{B} + S + C + B + T}{2} \tag{2.1}$$

Hypercharge is a quantum number that combines isospin and flavor in a single charge operator [4]. The hypercharge is always conserved under strong interactions.

The hypercharge can be written as,

$$Y = \mathcal{B} + S + \frac{C - B + T}{3} \tag{2.2}$$

2.1.4 Hadrons

Hadrons are composite systems made up of quarks. Standard hadrons are classified based on their quark content into two categories: $q\bar{q}$, known as mesons, and qqq or

$\bar{q}\bar{q}\bar{q}$, known as baryons. As illustrated in Figure 2.2, mesons are composed of two quarks, whereas baryons consist of three quarks. Additionally, bound states with more than three quarks exist, referred to as "exotic hadrons." These exotic hadrons are unstable and decay rapidly into more stable particles.

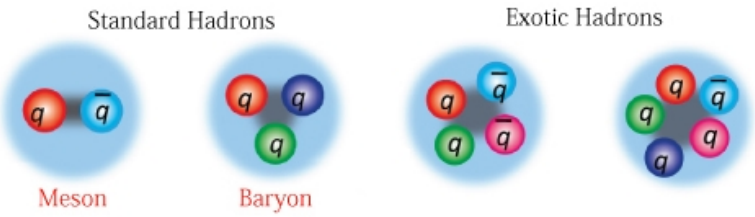


Figure 2.2: Bound states of hadrons.

2.1.4.1 Mesons

Mesons have a baryon number $\mathcal{B} = 0$ and consist of two quarks. They form a bound state of one quark and one antiquark ($q\bar{q}$). The quark flavors in the bound state can be different.

Light mesons, which contain u, d, and s quarks, follow SU(3) symmetry and have nine possible $q\bar{q}$ combinations, forming a nonet. These light mesons constitute an octet and a singlet, with the singlet positioned at the center of the octet (Figure 2.3).

$$3 \otimes \overline{3} = 8 \oplus 1 \tag{2.3}$$

For light mesons, where $C = B = T = 0$, equations 2.1 and 2.2 simplify to:

$$Q = I_3 + \frac{\mathcal{B} + S}{2} \tag{2.4}$$

$$Y = \mathcal{B} + S \tag{2.5}$$

By combining equations 2.4 and 2.5, a relationship between electric charge and hypercharge can be derived specifically for light mesons:

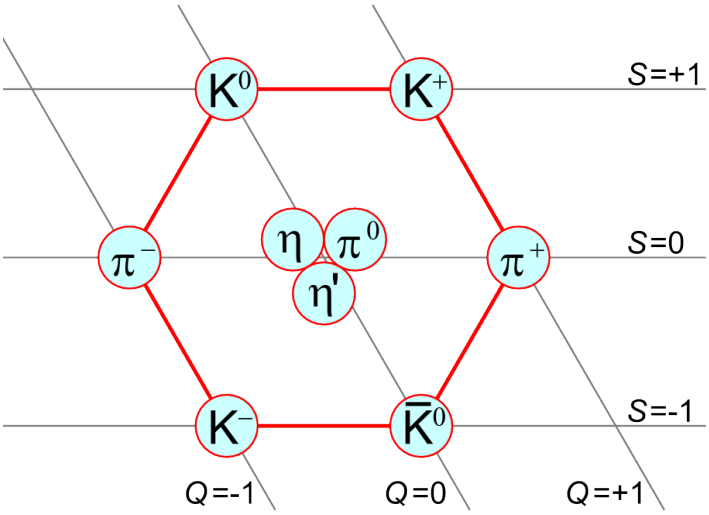


Figure 2.3: SU(3) weigth diagram for light mesons forming a nonet.

$$Q = I_3 + \frac{Y}{2} \tag{2.6}$$

In the DsTau experiment, charmed mesons are of particular interest. SU(3) symmetry is extended to SU(4) to include the charm quark. The SU(4) group (Figure 2.4) comprises 16 mesons, forming a 15-plet and a singlet.

$$4 \otimes \overline{4} = 15 \oplus 1 \tag{2.7}$$

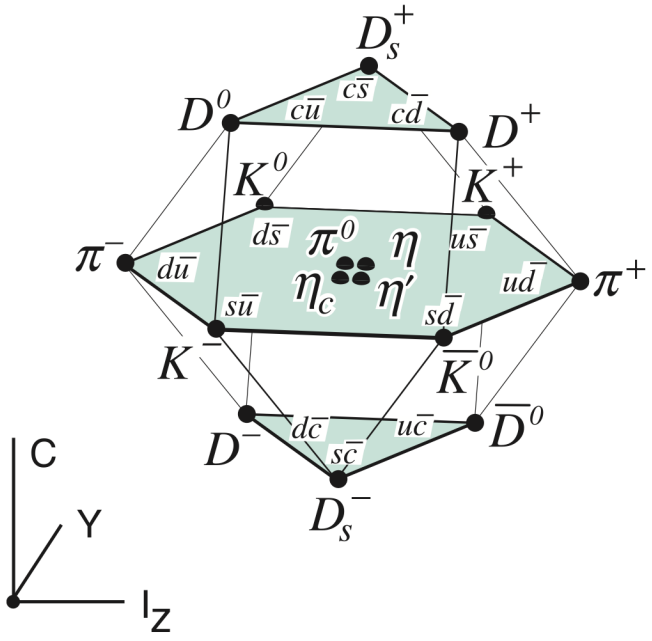


Figure 2.4: SU(4) weigth diagram for light mesons forming a 16-plet.

For the SU(4) group, which includes u, d, s, and c quarks, where $B = T = 0$, the hypercharge (Y) can be expressed as:

$$Y = \mathcal{B} + S - \frac{C}{3} \tag{2.8}$$

2.1.4.2 Baryons

Baryons form bound state with three quark (qqq) or three anti-quark ($\bar{q}\bar{q}\bar{q}$). All three quarks can have different flavors. For (qqq) state $\mathcal{B} = 1$ and for ($\bar{q}\bar{q}\bar{q}$) state $\mathcal{B} = -1$. Light baryons (quark content: u, d, and s) can be represented with SU(3) group.

$$3 \otimes 3 \otimes 3 = 10_S \oplus 8_M \oplus 8_M \oplus 1_A \tag{2.9}$$

Where subscript S is symmetric, M is mixed-symmetric, and A is anti-symmetric.

Similar to mesons SU(4) multiplets will be formed, if charmed baryons are included (Figure 2.5).

$$4 \otimes 4 \otimes 4 = 20_S \oplus 20_M \oplus 20_M \oplus 4_A \tag{2.10}$$

$$4 \otimes \overline{4} = 15 \oplus 1 \tag{2.11}$$

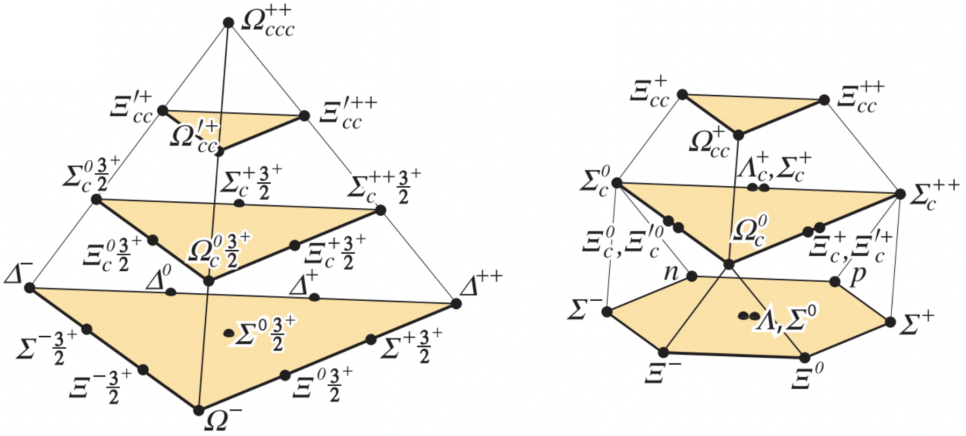


Figure 2.5: SU(4) weigth diagrams for baryons [7]. Symmetric 20-plet (left), mixed-symmetric 20-plet (right).

2.2 Charm hadroproduction

The D_s ($c\bar{s}$) meson is a type of charmed meson produced through a process known as charm hadroproduction [10]. Since the DsTau experiment aims to understand the differential production cross-section of D_s mesons, it is essential to study their production first.

Charm hadroproduction involves three main steps. The first step consists of the collision of high-energy hadrons. Due to their high momenta, these colliding hadrons can be considered collections of free partons. Essentially, these free partons come together and interact with each other.

In the second step, a Quantum Chromodynamics (QCD) process occurs. The simplest and most significant process is the first-order process, known as the fusion process. In

this process, a quark (q) and an antiquark ($\bar{q}$) annihilate to form a charm (c) and anti-charm ($\bar{c}$) pair, or two gluons (gg) interact to produce a $c\bar{c}$ pair. The $q\bar{q}$ annihilation occurs only via the s-channel, while the gg process can occur through the s, t, and u channels (Figure 2.6). There are also other processes for charm production, including higher-order perturbative QCD and flavor excitation processes.

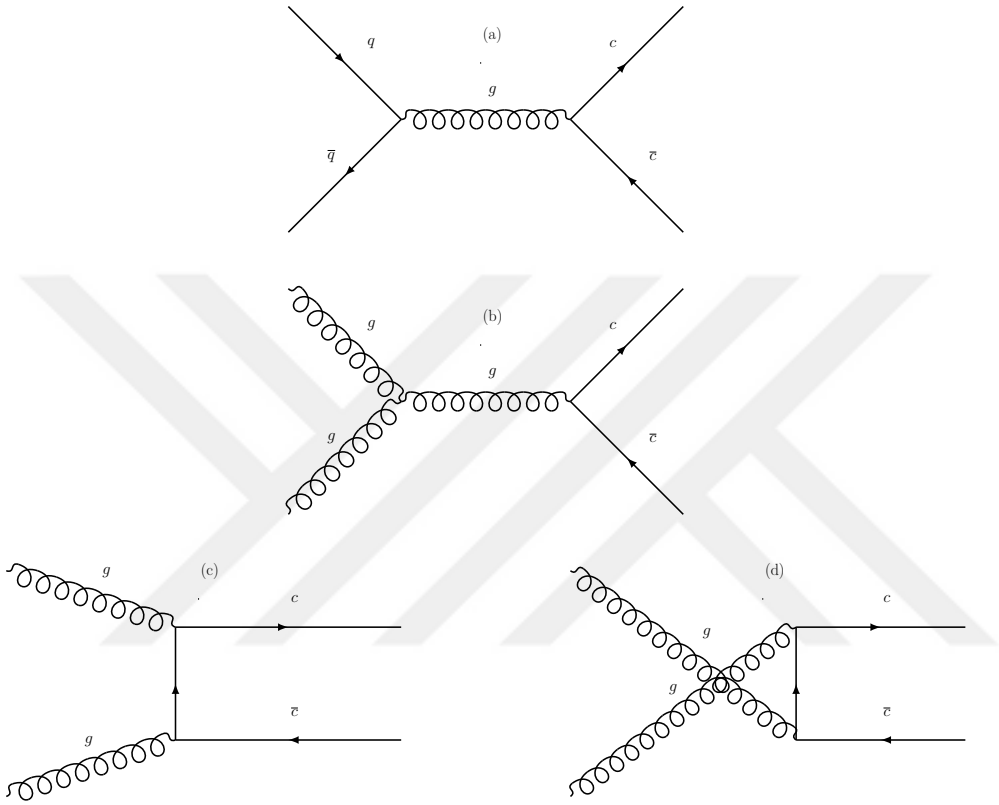


Figure 2.6: Feynman diagrams of the QCD fusion process. (a) $q\bar{q}$ s-channel process, (b) gg s-channel process, (c) gg t-channel process, and (d) gg u-channel process.

The third step is the hadronization process. During this step, the produced charm quarks form bound states with other quarks through the strong force. As a result, charmed hadrons are formed, such as D^+, D^-, D^0, D_s^-, D_s^+, Λ_c^+, and Ξ_c^+.

2.3 D_s Meson Decay

The D_s meson, produced after charm hadroproduction, is unstable and has a relatively short mean lifetime of $501.2 \pm 2.2 \times 10^{-15}$ s. The DsTau experiment aims to explore these decay processes. As Figure 2.6 illustrates, the D_s meson can decay through purely leptonic, semi-leptonic, and hadronic channels [8]. Among these, hadronic decays are predominant, surpassing the sum of leptonic and semi-leptonic decays (Figure 2.7). Specifically, while 18% of the decay channels are leptonic and semi-leptonic, a significant 69.9% are hadronic.

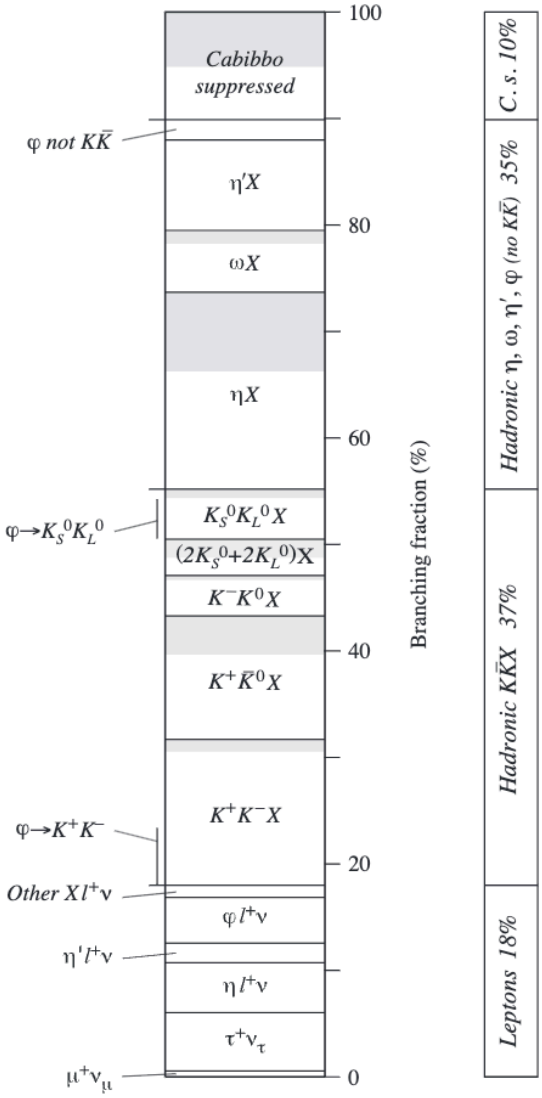


Figure 2.7: D_s^+ branching fractions.

2.3.1 Pure Leptonic Decays

In purely leptonic decays, the decay products of the D_s meson only consist of leptons and their corresponding neutrinos.

1. $D_s^+ \to \tau^+ \nu_\tau$ (5.36%)
2. $D_s^+ \to \mu^+ \nu_\mu$ (0.53%)
3. $D_s^+ \to e^+ \nu_e$ $(< 0.08\%)$

The decay $D_s^+ \to \tau^+ \nu_\tau$ has the highest branching ratio, making the D_s^+ an excellent candidate for studying ν_τ. Feynman diagram of $D_s^+ \to \tau \nu_\tau$ decay is illustrated as an example of pure leptonic D_s meson decay (Figure 2.8).

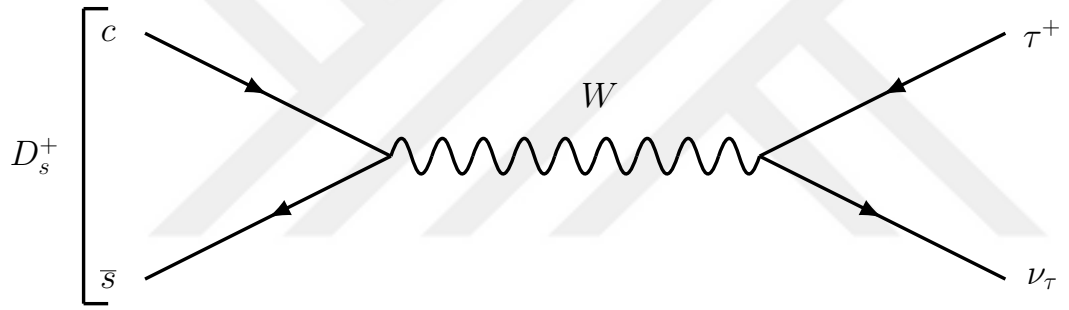


Figure 2.8: $D_s^+ \to \tau \nu_\tau$ decay.

2.3.2 Semi-leptonic Decays

The sum of all semi-leptonic decay modes constitutes only 6.0% of all decay modes. Semi-leptonic decays involve one lepton, its associated neutrino, and a hadron.

1. $D_s^+ \to X\tau^+\nu_\tau$ (6.0 %)

Here, X denotes any hadron products present in the semi-leptonic modes, with X mostly comprising the ϕ meson. Figure 2.9 illustrates an example of the semi-leptonic decay process $D_s^+ \to \phi^0 e\nu_e$.

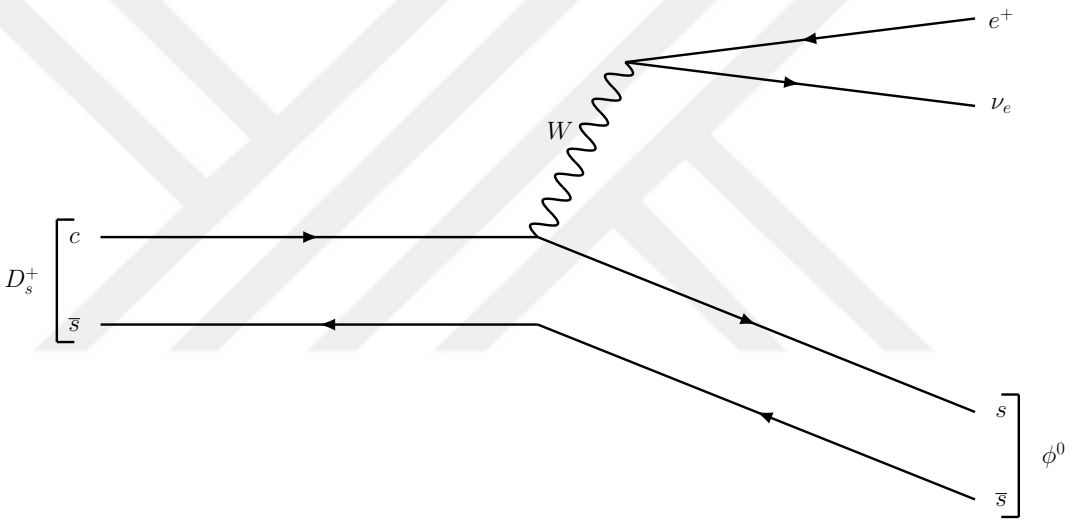


Figure 2.9: $D_s^+ \to \phi^0 e\nu_e$ decay.

2.3.3 Pure Hadronic Decays

Hadronic decays only consist of hadron productions. The pure hadronic decay modes of the D_s can be categorized into two groups: those containing Kaon meson pairs ($K\bar{K}$) and those without any $K\bar{K}$ pairs.

1. $D_s^+ \to XK\bar{K}$ (inclusive $K\bar{K}$ pairs) (35.2%)
2. $D_s^+ \to X$ (no $K\bar{K}$ pairs) (34.7%)

In this context, X represents any hadron products found in the hadronic decay modes. In Figure 2.10, the decay process $D_s^+ \to K^+K^0$ is illustrated as an example of a purely hadronic decay.

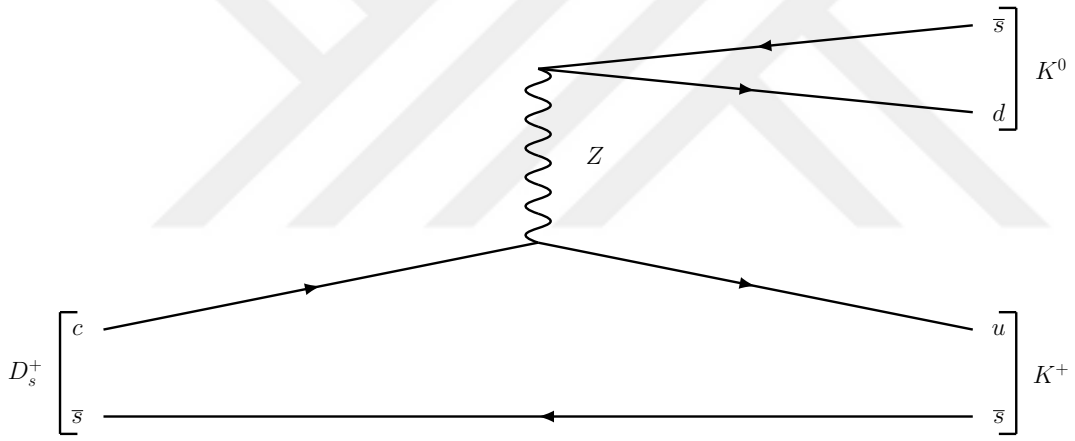


Figure 2.10: $D_s^+ \to K^+K^0$ decay.

CHAPTER 3

THE DSTAU EXPERIMENT

3.1 Motivation of the Experiment

Tau neutrinos (ν_τ) are primarily produced through two mechanisms: neutrino oscillations, which have been extensively studied in long baseline experiments such as OPERA [11], MINOS [13], and T2K [12], and D_s meson decays, previously investigated in the DONuT [14] experiment Figure 3.1. The DONuT experiment measured the ν_τ production cross section but with significant uncertainty due to the limited number of observed ν_τ events, totaling only nine.

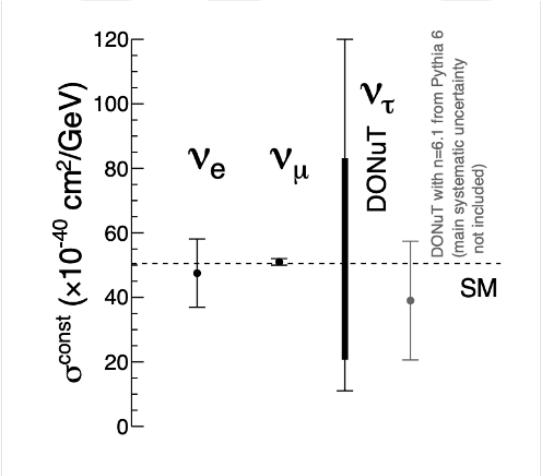


Figure 3.1: Cross section of three neutrino flavors. The Standard Model prediction is indicated as dashed line.

The DsTau [15] experiment aims to measure the differential production cross section of D_s mesons in 400 GeV proton-nucleus interactions on tungsten and molybdenum targets to reduce the significant uncertainty in ν_τ production. By studying 10^3 D_s to

τ decays, the experiment intends to enhance the understanding of the D_s production mechanism, thereby decreasing the previously measured 50% systematic error in the ν_τ production cross section to approximately 10%.

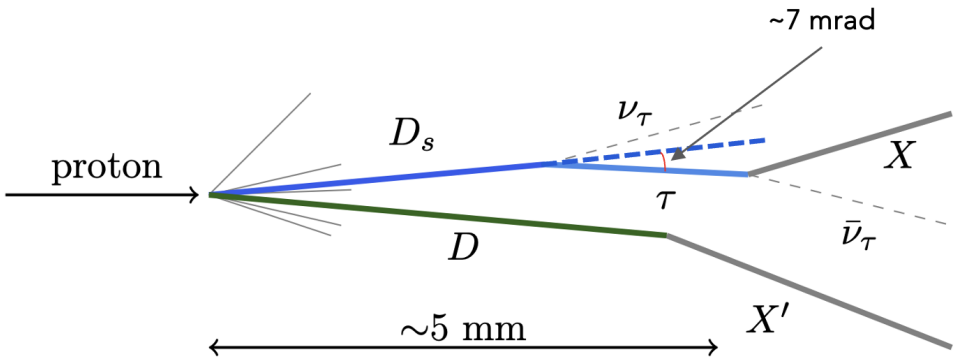


Figure 3.2: Double kink topology of $D_s \to \tau \to \nu_\tau$.

The D_s to τ decay topology is illustrated in the Figure 3.2. Initially, the D_s meson decays into a τ lepton and a ν_τ, followed by the decay of the τ lepton into another $\bar{\nu_\tau}$. This sequence is referred to as a double kink topology. The flight lengths of the D_s and τ decays are 3.3 mm and 2.0 mm, respectively, with the kink angle of the D_s to τ decay being only seven milliradians. Consequently, an extremely high-resolution detector is required to measure such a small angle accurately. Nuclear emulsions with a sub-micron spatial and sub-mrad angular resolutions are used to meet the experiment's high-resolution requirements.

3.2 Experimental Setup

The DsTau experiment is a fixed target experiment. Hence, targets and emulsion films are intertwined, allowing the detector to capture short-lived particles such as D_s mesons. Tungsten and molybdenum plates are used as targets during the physics run.

The detector structure consists of emulsion plates, tungsten plates, and plastic spacers. Emulsion plates are used for particle detection; tungsten is a dense medium for interacting with the incoming proton beam, and plastic spacers function as the decay

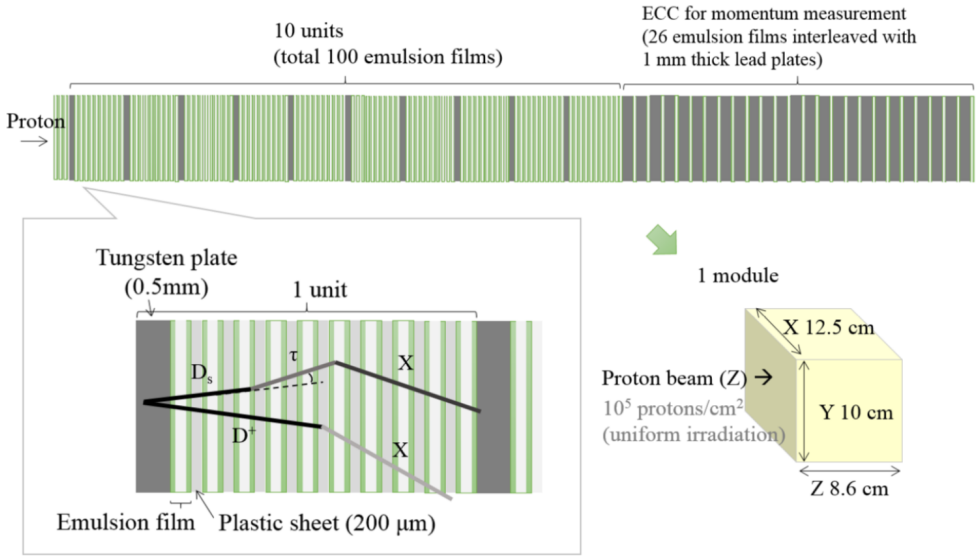


Figure 3.3: Schematic view of test run DsTau detector.

volume Figure 3.3.

The tungsten plates have an approximate thickness of 500 micron, with each unit consisting of two tungsten plates interspaced with ten 320-micron-thick emulsion plates and nine 200-micron-thick plastic sheets. This assembly is referred to as a unit, and the DsTau detector contains ten such units, resulting in ten tungsten plates and 100 emulsion plates. Additionally, five emulsion plates are positioned in front of the module to detect and analyze the characteristics of incoming proton beams. The transverse dimensions of the detector module were 12.5 cm x 10 cm during the test run, but in subsequent runs, module sizes were enlarged to 20 cm x 25 cm.

Downstream of the module is the Emulsion Cloud Chamber (ECC), designed for momentum measurement utilizing the Multiple Coulomb Scattering (MCS) technique. The ECC comprises 26 lead targets, each 1 mm thick, interleaved with emulsion films. This structure was modified after the test run due to inefficiencies in the track reconstruction process caused by high track density within the ECC unit, as shown in Figure 3.4. The high track density, caused by electromagnetic showers, was due to the ECC unit's high density [16].

Modifications were implemented to reduce the high track density in the ECC. The

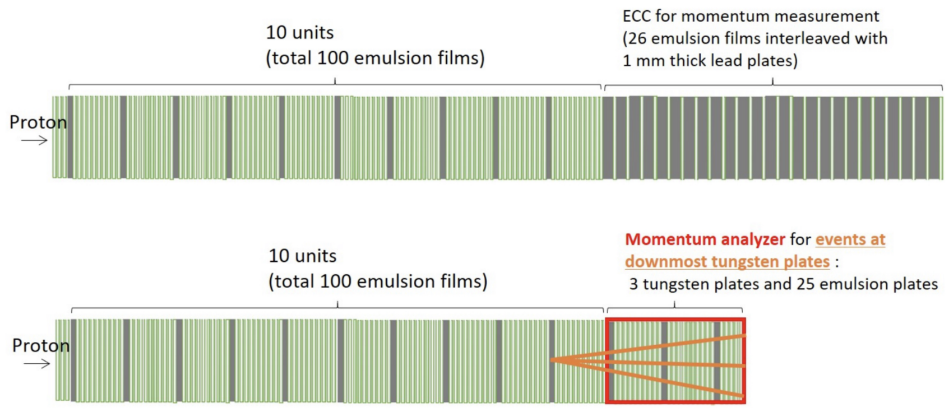


Figure 3.4: Previous detector configuration used during the test run with a lead target ECC (top). Current detector configuration in use with a tungsten target ECC (bottom).

26 lead plates were replaced with three 0.5 mm thick tungsten plates, and the total number of emulsion plates was reduced to twenty-five Figure 2.6. These adjustments in the new ECC unit improved the emulsion film's efficiency and scanning speed [17].

3.3 Nuclear Emulsion Films

As previously discussed, the DsTau detector utilizes the nuclear emulsion technique. An emulsion plate comprises 70-micron-thick emulsion layers on both sides of a 210-micron-thick plastic base, enabling the reconstruction of base-tracks within the plastic base during the track reconstruction phase Figure 3.5.

Nuclear emulsion films are composed of silver halide crystals Figure 3.2 embedded in a gelatin binder. When a charged particle passes through the emulsion film, the crystals along the particle's trajectory become opaque black Figure 3.5. This allows the particle's track within the emulsion medium to be captured and analyzed later. Unlike other particle detectors, emulsion films function as detectors and storage units, as the activated silver halide crystals preserve their state when subjected to an appropriate development process.

As previously mentioned, emulsion films are sensitive to charged particles and photons. Emulsion films are kept within aluminum sheets from production until the de-

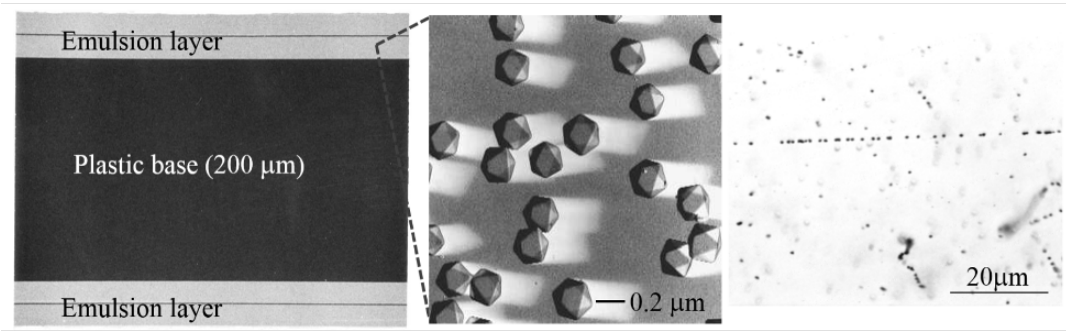


Figure 3.5: Left: Composite structure of an emulsion plate. Middle: Silver halide crystals embedded within the nuclear emulsion. Right: Microscopic image of a particle track.

velopment phase to prevent background effects.

Exposure to light can damage particle tracks within the emulsion film; therefore, the entire development process is conducted in a darkroom. A series of chemical processes, known as development, are required to examine the particle tracks under a microscope. Initially, the grains are enlarged to enable easy scanning under a microscope. Subsequently, the grains are stabilized and fixed to prevent further exposure to charged particles, allowing the emulsion films to be scanned accurately.

3.4 Target Mover

The SPS can deliver 10^5 protons per spill over 4 seconds. However, there is a limit to the track density required for proper track analysis. Consequently, the proton beam can only irradiate a small portion of the emulsion plate at a time. The module is mounted on a motorized unit known as a target mover [18], which moves along the X-Y axis to irradiate the entire module surface. During the beam spill, the target mover remains stationary, and during the SPS cooldown, it advances to the next area for irradiation in the subsequent spill Figure 3.6.

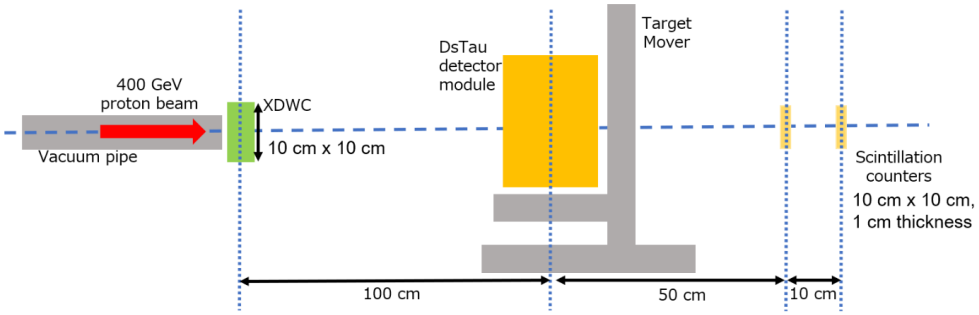


Figure 3.6: Schematics of the target mover.

3.5 Emulsion Scanning

An automated nuclear emulsion read-out system known as the Hyper Track Selector [19] (HTS) (Figure 3.7) is utilized for emulsion scanning. Located at Nagoya University in Japan, the HTS has been employed in numerous previous experiments and will continue to be used in upcoming emulsion-based experiments. With its current configurations, the HTS can scan emulsion films at a speed of 5000 cm^2 per hour.

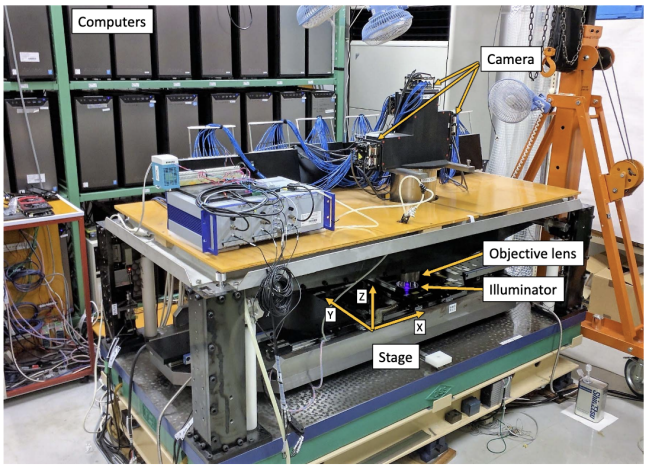


Figure 3.7: A photograph of the Hyper Track Selector.

An emulsion film records particle trajectories with three-dimensionally aligned silver grains. Using the HTS, a tomographic image of the emulsion plates is captured, and these silver grains are linked together using a track-finding algorithm called "Track Selector" Figure 3.8.

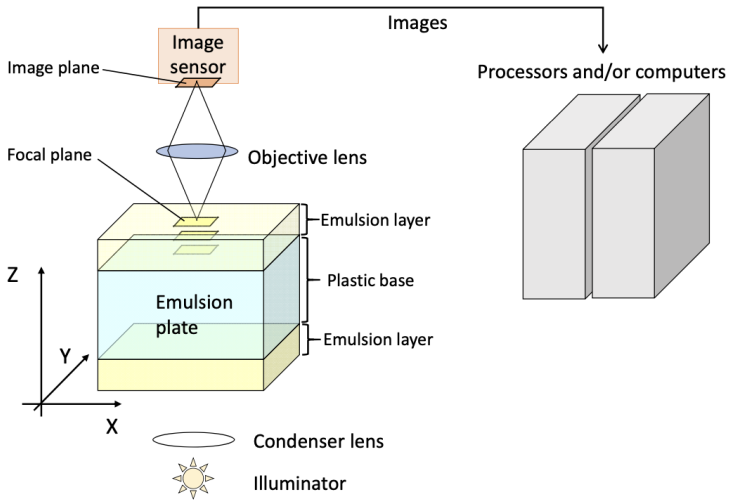


Figure 3.8: A schematics of automated nuclear emulsion scanning system.

In the Track Selector process, twenty-two tomographic images of the emulsion plates are captured at varying depths by adjusting the lens focal length. These images are then transferred to a computer, where micro-tracks are reconstructed on both sides of the emulsion films. Micro-tracks from both ends are linked to form a base-track within the plastic base. The efficiency of base-track reconstruction is measured to be greater than 95%, but it decreases downstream due to increased track density.

CHAPTER 4

DATA RECONSTRUCTION AND ANALYSIS

4.1 Reconstruction

The DsTau software is utilized to analyze the DsTau emulsion film. The entire plate is divided into smaller sections to manage the extensive dataset generated by the DsTau experiment, enabling more efficient and fast computer processing and analysis. The detector module is divided along both the transverse and depth axes (Figure 4.1). The transverse axis is partitioned into 63 regions, referred to as sub-areas. The depth axis is divided into eight sections, known as sub-volumes. Each sub-volume is designed to overlap with adjacent sub-volumes to ensure the continuity of particle tracks. Each sub-volume contains three tungsten plates and 30 emulsion plates, except the first sub-volume, which includes an additional five emulsion plates at the beginning of the detector module.

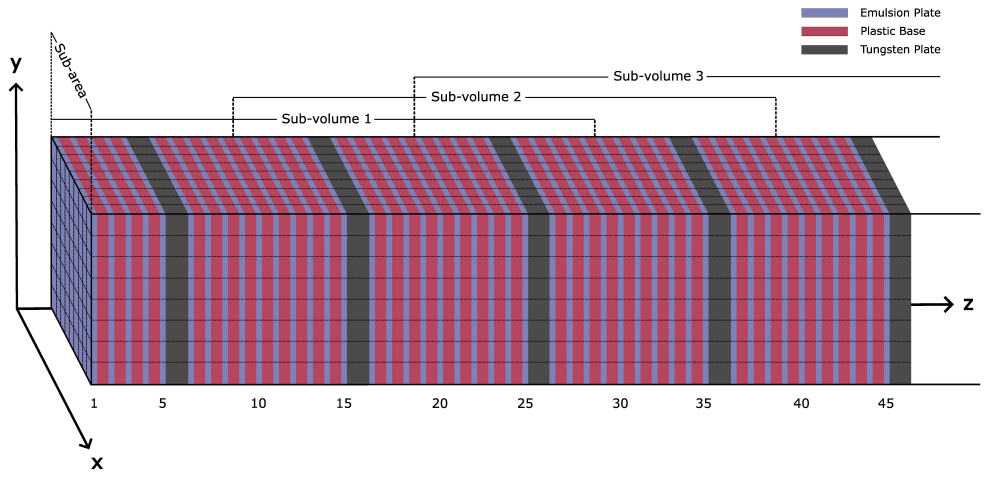


Figure 4.1: Representation of sub-areas and sub-volumes.

The DsTau analysis procedure consists of six steps: base-track reconstruction, fine alignment, volume-track reconstruction, proton linking, vertexing, and data conversion to ROOT format (Figure 4.2).

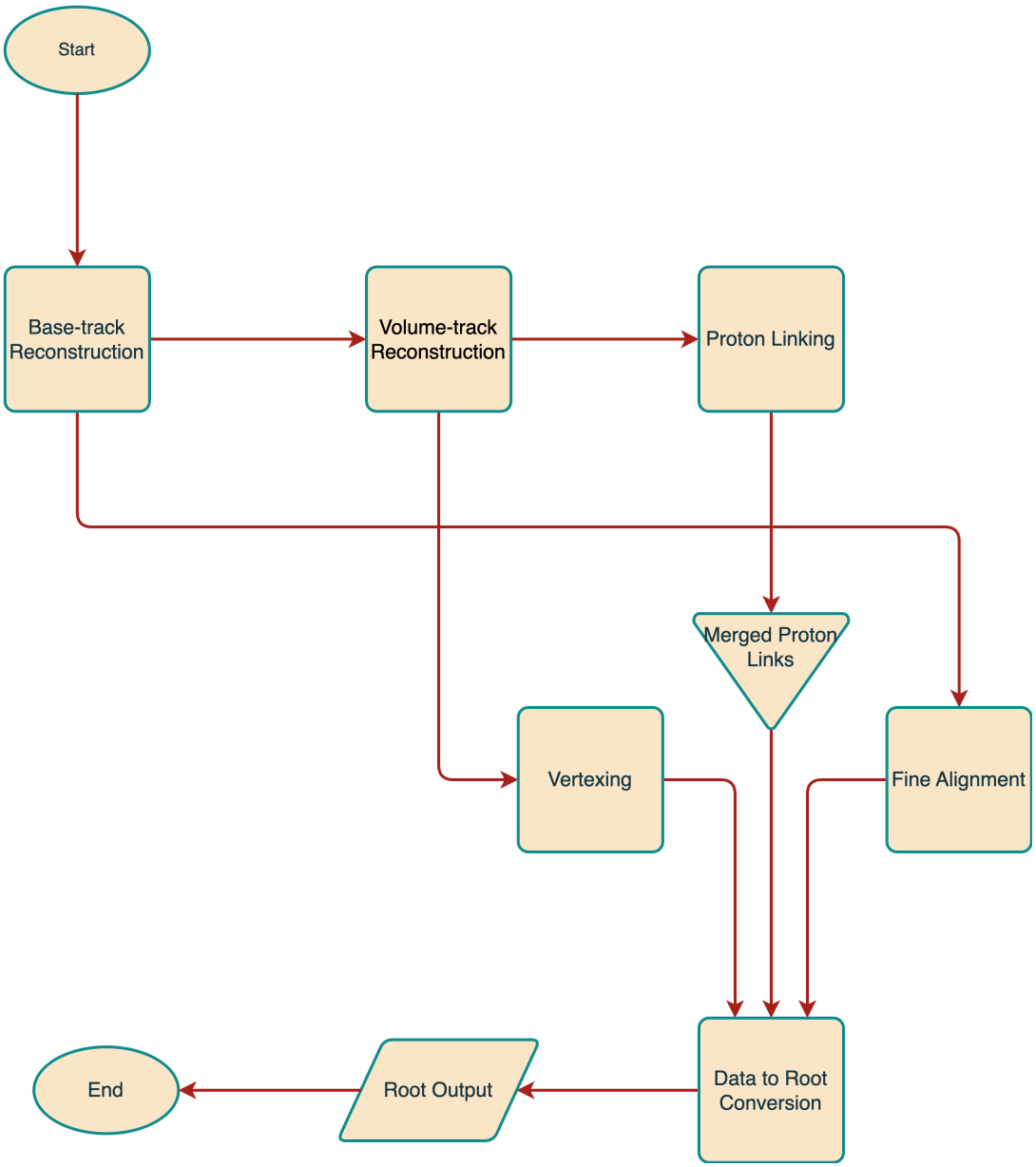


Figure 4.2: Flowchart of DsTau reconstruction.

4.1.1 Base-track reconstruction

Emulsion plates consist of emulsion films separated by a plastic base. Charged particles create traces on the emulsion films located at both ends of the emulsion plates. These traces, called micro-tracks, are scanned using a microscope and transferred to a computer. A longer base-track is constructed using the micro-tracks from both emulsion films (Figure 4.3). These longer tracks are called base-tracks because the new track is constructed at the center of the plastic base.

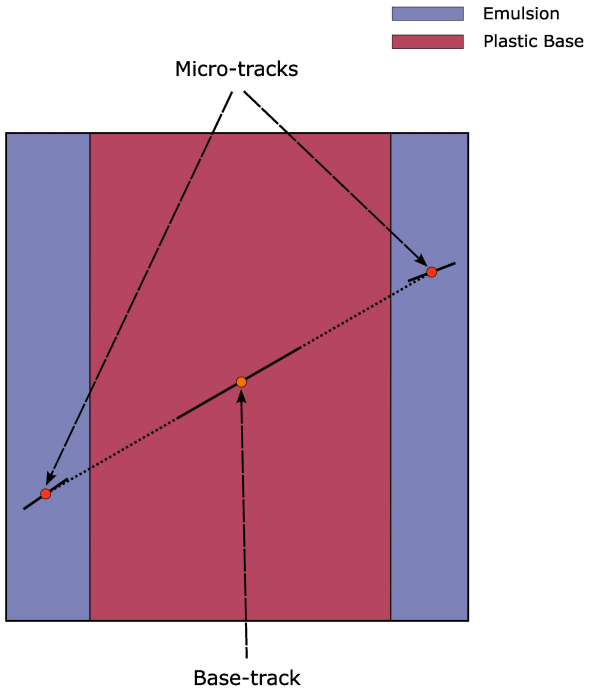


Figure 4.3: Base-track reconstruction process.

4.1.2 Fine alignment

Each emulsion film is scanned individually with a microscope, leading to readouts in different local reference frames. Consequently, before connecting base-tracks, a fine alignment procedure must be applied to each film. This procedure ensures that the spatial components of the emulsion readouts are accurately converted to a global reference frame.

4.1.3 Volume-track reconstruction

A tracking algorithm (Figure 4.4) is applied to connect consecutive base-tracks which are linked together, resulting in the construction of longer volume-tracks.

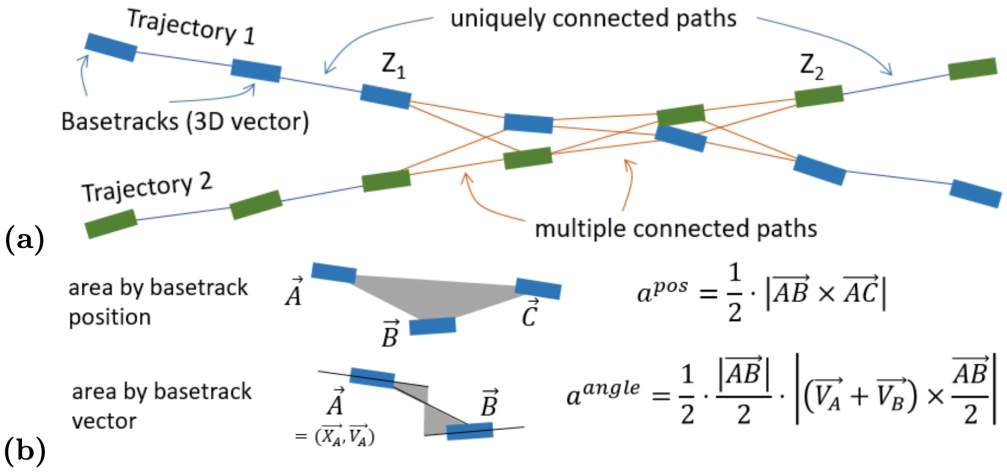


Figure 4.4: (a) Two tracks converging in a high-density environment. (b) Visualization of the calculation of a^{pos} and a^{angle}.

In the high-density environment of the DsTau experiment, standard tracking algorithms may fail to perform effectively. Consequently, a new tracking algorithm has been developed specifically to reconstruct tracks in these high-density regions (Figure 4.4). When the algorithm encounters multiple track candidates, as illustrated in the diagram, it keeps all potential path candidates. Subsequently, it calculates position-based (a^{pos}) and angle-based (a^{angle}) areas for each possible path.

$$a^{average} = \left(\sum_{i}^{n-2} a^{pos} + \sum_{i}^{n-1} a^{angle} \right) / (n - 0.5) \tag{4.1}$$

The average area ($a^{average}$) for each selected path is calculated using the provided formula 4.1. The path with the smallest $a^{average}$ is chosen as the true path among all the path candidates.

4.1.4 Proton Linking

As mentioned at the beginning of the chapter, data is divided into smaller datasets to process experimental data efficiently. This approach allows for effective data analysis but comes with certain drawbacks. After the reconstruction process, the sub-areas need to be merged again. This merging can cause overlaps at the borders, potentially compromising data quality. Another issue arises from the beam angle of the beam protons; since this angle in the experimental data is not zero, some tracks may cross into other sub-areas. Consequently, these tracks must be excluded from the reconstructed data.

Additionally, once the data is divided into sub-volumes, it becomes impossible to determine the origin of tracks localized within a sub-volume. This limitation makes it difficult to identify primary protons and higher-order interactions beyond the first sub-volume. A method called proton linking has been developed to address these challenges, in addition to the standard reconstruction methods used in emulsion analysis.

The proton linking algorithm comprises three distinct components: the proton selection, the track linking, and the segment linking 4.6.

4.1.4.1 Proton Selection

The proton linking method initiates with proton selection, which is determined based on the angular orientation of the tracks. Initially, the angles of the tracks are derived from a linear fit of the segment positions, provided that each track comprises a minimum of three segments within the detector module. Subsequently, the derived track slopes are filled into a histogram, and a Gaussian fit is applied. The parameters obtained from this fit are then utilized for the proton selection Figure 4.5.

As the figure 4.6 illustrates, proton selection is performed within the emulsion plates ranging from 0 to 4.

The following selection criteria are used for the initial proton selection.

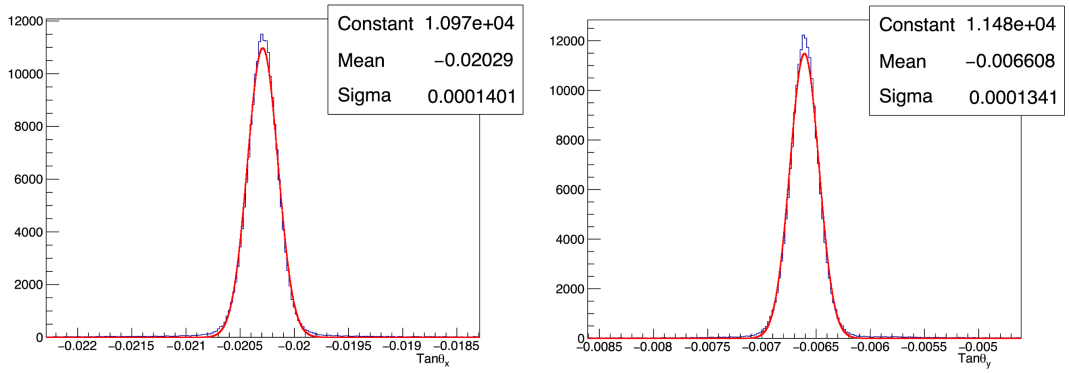


Figure 4.5: The distribution of proton track angles in the XZ and YZ planes is presented, and a Gaussian fit is applied. The region within 3-sigma is considered the primary proton track.

- Since primary protons are incident upon the detector, tracks must include a segment within the first three emulsion plates of a module.
- Tracks are required to contain at least three segments within the first five emulsion plates to facilitate the application of a linear fit to the segments.
- Since incoming proton beams mostly have a similar angular distribution around the beam angle, tracks falling within the 3-sigma slope range are identified as protons, and those outside that range are assumed as backgrounds.

4.1.4.2 Track Linking

Tracks identified through the proton selection method are traced to the end of the sub-volume using the track linking method as seen on the horizontal dashed line in the Figure 4.6. This method employs the TrackID, a unique identification number assigned to each track. The TrackID remains consistent across all segments belonging to the same track. By searching for proton tracks in subsequent segments, one can trace the track segments to the end of the module. However, given the vast number of segments within a single module, directly employing this method is impractical.

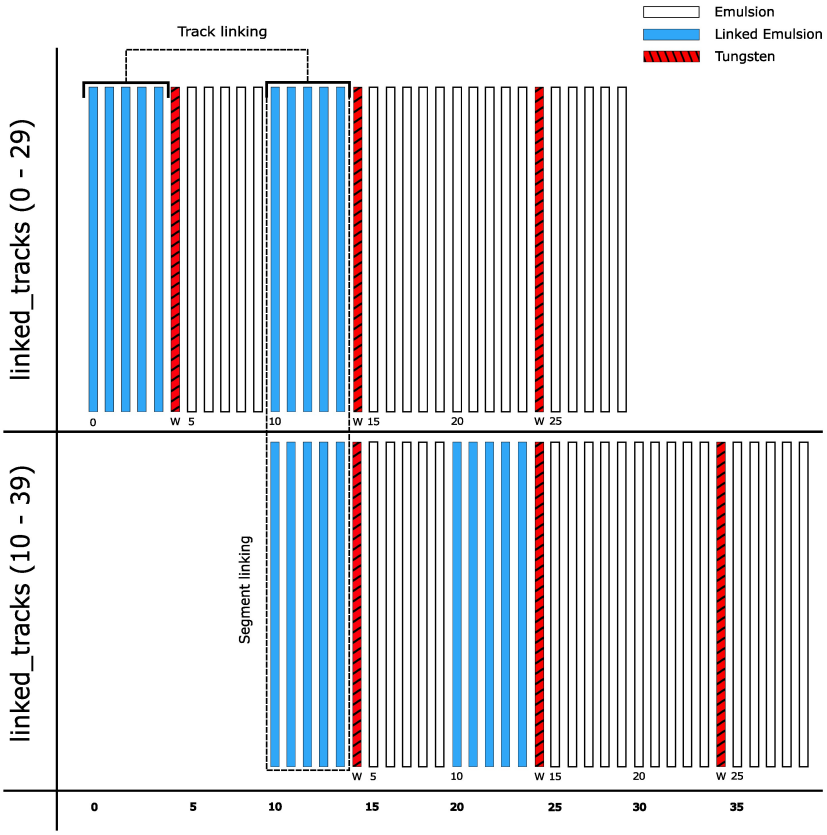


Figure 4.6: Visualization of the proton linking method. The upper section displays the first sub-volume, while the lower section presents the second sub-volume.

The module is divided into two sections to optimize the process: upstream and downstream. The upstream section covers the first five emulsion plates up to the initial tungsten plate, while the downstream section includes the five emulsion plates preceding the second tungsten plate. The choice to use a five-emulsion-plate tracking

algorithm arises from the fact that the reconstruction process is not flawless. Some tracks may have missing segments. An array of segments is used to address this issue instead of relying on a single segment. The TrackIDs of all segments within the upstream section are dumped into a vector, from which unique TrackIDs are selected to reduce complexity. These unique TrackIDs are then searched within the downstream segment's TrackIDs using search algorithms. The resulting TrackIDs, along with the spatial components of the tracks, are written separately in a file for the upstream and downstream sections. One can determine the tracks that have interacted by identifying any missing TrackIDs between two files.

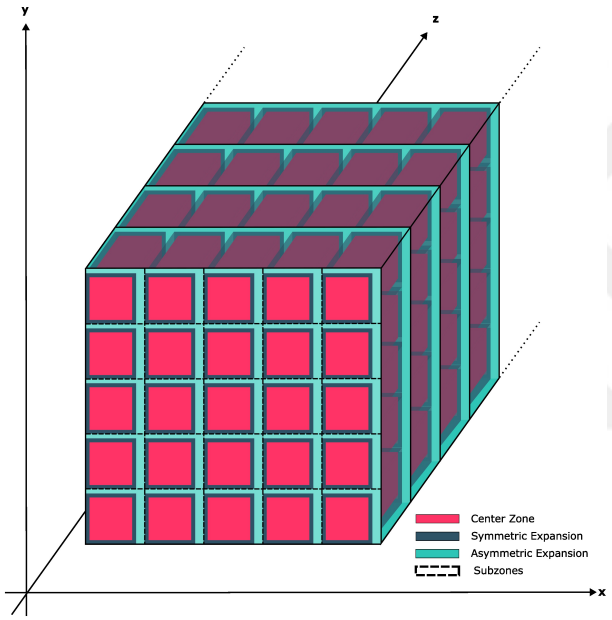


Figure 4.7: 3D representation of sub-zones with transition area.

Despite these enhancements in efficiency, the method remains too complex to be processed effectively. Consequently, the sub-areas are further divided into smaller regions known as sub-zones (Figure 4.7), each measuring 4000 micrometers along both the x and y axes. The optimal approach involves working with twenty-five sub-zones arranged in a 5x5 grid. Given the limitations of resources in CERN's HTCondor batch system, five horizontal processes are executed in parallel. Once these parallel processes are completed, the next set of five horizontal zones is processed sequentially (4.8). This approach significantly improves processing times.

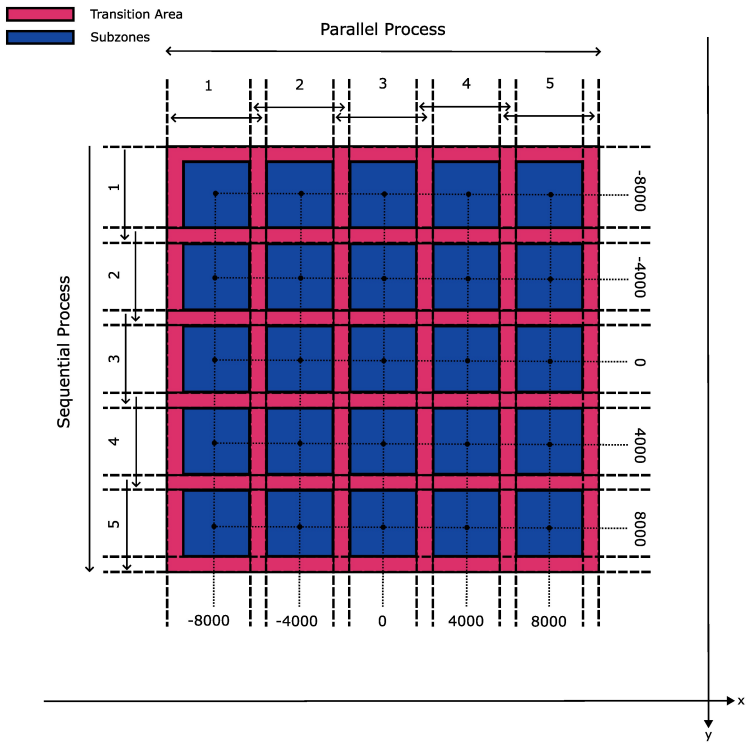


Figure 4.8: Sequential stages of the proton linking process. Double-headed arrows indicate parallel processes, while single-headed arrows denote sequential processes and their directions.

However, dividing the area into sub-zones presents two challenges. First, once the processing is complete, all data must be reassembled. Second, particles near the edges of sub-zones may cross into adjacent sub-zones at the downstream, potentially creating the false impression that the particle interacted at an incorrect location (Figure 4.9). To address this issue, sub-zones are extrapolated along the beam angle of the incident protons (red region in Figure 4.10) rather than directly along the depth axis, thereby minimizing proton exclusion. Additionally, sub-zones are expanded along the transverse axis to capture tracks with larger angles. This expanded region is referred to as the transition area, consisting of two distinct expansion methods.

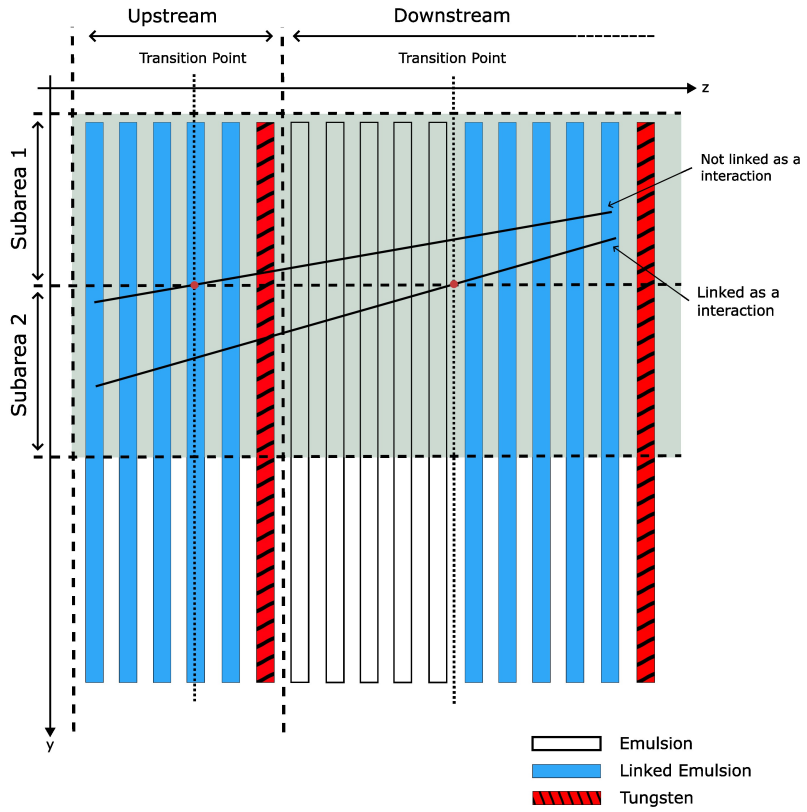


Figure 4.9: An illustration of tracks transitioning to an adjacent sub-area.

Symmetrical Expansion: The 5-sigma region of the proton track distribution is determined and then multiplied by the distance between the upstream and downstream tungsten plates. This value symmetrically expands the transition area along the x and y axes (dark blue region in Figure 4.10). Consequently, all selected protons, even those with larger track slopes, are captured.

Asymmetrical Expansion: Given that each sub-area is irradiated individually, resulting in different beam angles for each sub-volume, the transition area is expanded asymmetrically along the beam axis direction (teal region in Figure 4.10). This adjustment is made based on the variations in beam angles across different sub-areas.

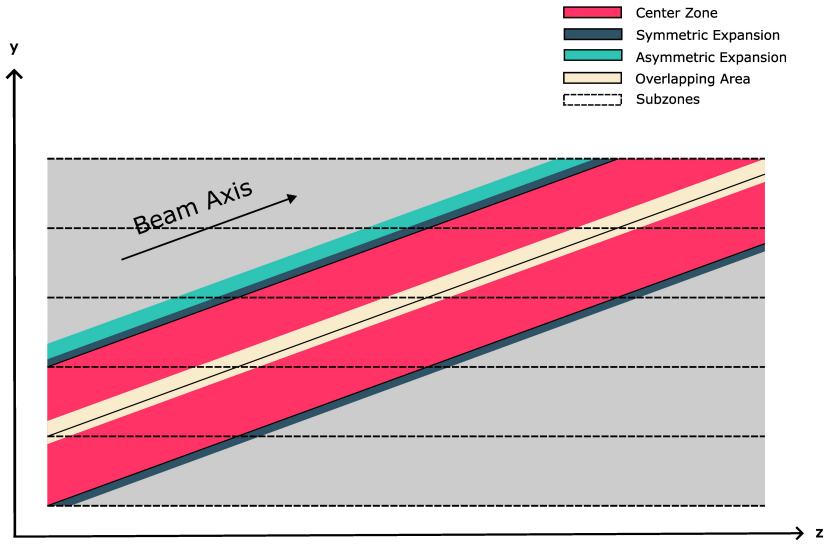


Figure 4.10: A lateral cross-section of the sub-volume is illustrated. Dashed lines indicate the sub-zones and the colored regions aligned with the beam axis represent the sub-zones after extrapolation.

4.1.4.3 Segment Linking

Each sub-volume contains a total of three tungsten plates. Therefore, to trace the tracks to the end of the module, it is necessary to continue linking across subsequent sub-volumes. Primary protons are tracked between sub-volumes using the segment linking method. Since each sub-volume is reconstructed independently, the TrackIDs for the same tracks differ between adjacent sub-volumes. However, another parameter, SegmentID, can be employed to track between sub-volumes. Similar to TrackIDs, SegmentIDs are unique identifiers assigned to segments. Unlike TrackIDs, SegmentIDs are unique to each plate and are independent of sub-volumes. Consequently, SegmentIDs can be used to follow track segments across different sub-volumes.

The segment linking process connects the segments of a track in the downstream portion of one sub-volume with the segments of the track in the upstream portion of the subsequent sub-volume as seen on the vertical dashed rectangle in the Figure 4.6. Each segment is individually linked across five emulsion plates. Following this linking, the TrackIDs of the connected tracks are compiled into a vector, and unique

TrackIDs are selected to avoid track duplication.

The efficiency of the reconstruction process decreases as one progresses downstream within the same sub-volume. Therefore, segment linking is performed before the second tungsten plate rather than before the third one.

4.1.4.4 Workflow

The proton linking process begins with estimating the mean and standard deviation of the track slope distribution derived from the linked track files, which are the output of the tracking algorithm. These extracted parameters are then input into the proton selection algorithm, and tracks that meet the selection criteria are identified as primary proton tracks. Both parameter extraction and proton selection are performed exclusively for the first sub-volume. Subsequently, the selected protons are tracked down to the beginning of the second tungsten plate within a sub-volume using the track linking method. The segment linking method is then employed to connect the tagged tracks to the next sub-volume, and unique tracks are identified. This sequential process of track linking and segment linking continues until the end of the module is reached. Upon completion of the entire process, the files from the sub-zones are merged and written into an output file.

Figure 4.11 presents a flowchart showing the proton linking method.

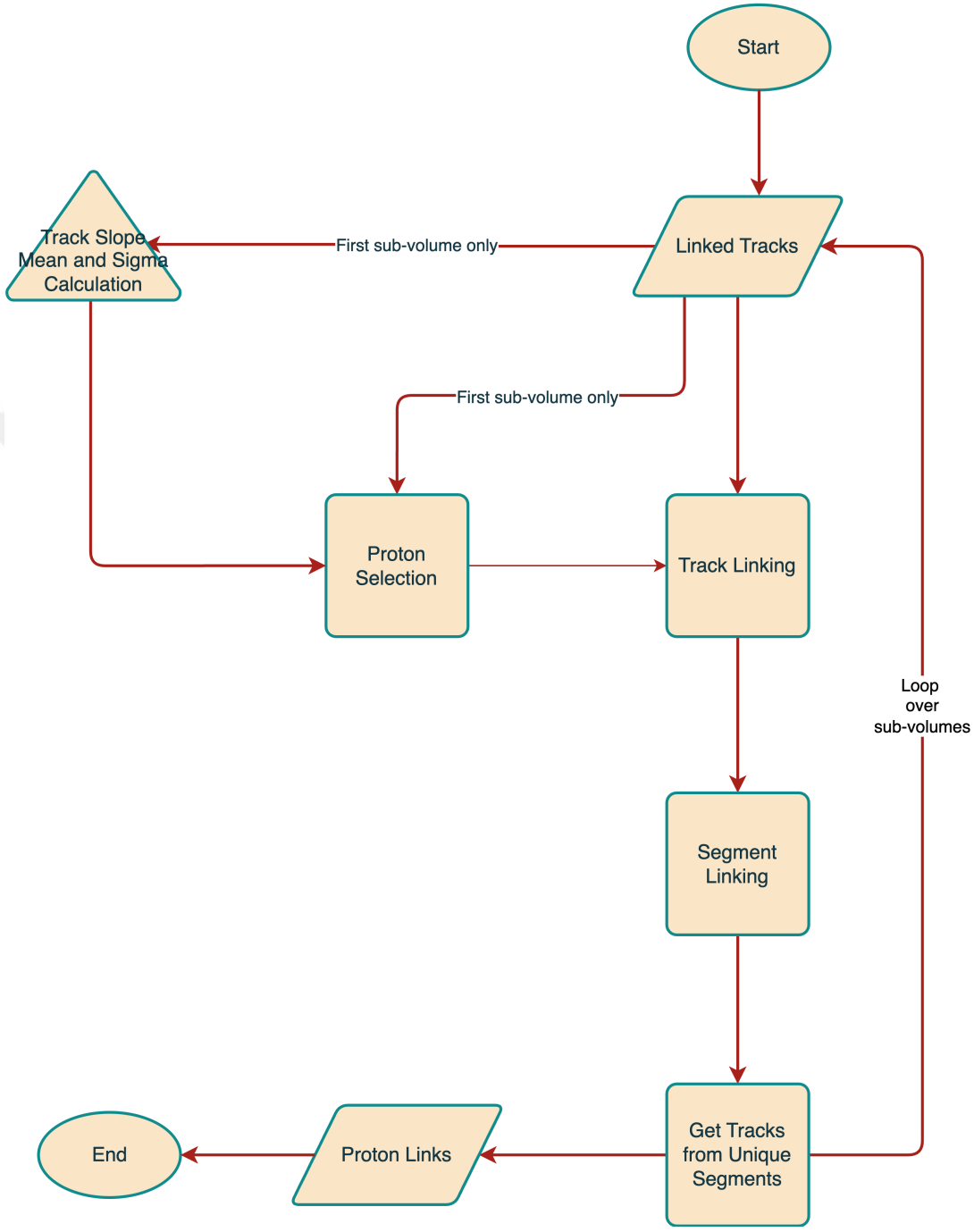


Figure 4.11: Proton linking flowchart.

4.1.5 Vertexing

At this reconstruction phase, reconstructed data only possesses local volume-tracks. The volume-tracks' potential interaction points (vertices) are reconstructed using the vertexing algorithm, and the selected daughter tracks are subsequently associated with these vertices.

A vertexing algorithm initially identifies a vertex point based on the parent track candidate. It then calculates the impact parameter, which is the distance between the vertex point and the origin of the daughter track, after extrapolating along the depth axis to the vertex point. Those candidates meeting the impact parameter selection criteria are designated daughters and added to the daughter bunch. The vertex position is determined by both the parent track and the origin points of the daughter tracks. Consequently, the position of the vertex point is updated after each successive attachment of daughter tracks.

4.1.6 Data conversion to ROOT format

Upon completion of the reconstruction process, three different output files are generated: fine alignment files, vertexing files, and proton link files (see three inputs to "Data to ROOT Conversion" node in the Figure 4.2). Fine alignment files contain the necessary corrections for vertices, ensuring that all vertices are transformed into a common global reference frame. Vertexing files include parent candidate tracks, vertices, and daughter tracks. Proton link files comprise TrackIDs, globally unique identifiers (GlobalTrackIDs), and the spatial parameters of the tracks, separately recorded for both the downstream and upstream sections.

Initially, the vertexing and proton link files are read sequentially for each sub-area. The TrackIDs from the proton link files are then compared with the parent track candidate TrackIDs. If both IDs match, the parent candidate is flagged as a primary proton track, and the corresponding vertex point is identified as a primary vertex. Due to the nature of vertexing algorithms, some vertices may be associated with multiple parent candidates. However, the proton linking method allows for accurately selecting the true parent track from the vertexing files. Consequently, after the matching process,

the correct parent track is selected.

Similar to the track linking method, some tracks may cross into adjacent sub-areas, potentially resulting in false interactions. However, unlike the track linking method, a transition area cannot be introduced for sub-areas because they are divided along the beam axis direction prior to the reconstruction process. Tracks are extrapolated to the end of the downstream section to address this issue. If a particle does not interact within the region and crosses into another sub-area, the parent tracks and their associated daughter tracks and vertex points are removed.

Finally, the fine alignment files are read, and each vertex point is transformed to a new position based on the provided parameters. Vertices near the tungsten plate's border may migrate into the emulsion or vice versa. Following the application of fine alignment, the interaction medium of some vertices is also updated. However, this method only partially resolves the migration issue, which will be discussed later in the chapter 4.3.5.

After applying this method to the data, all sub-areas are merged, and the proton link parameters, along with the updated vertexing parameters, are recorded in eight distinct root files, each corresponding to a specific sub-volume.

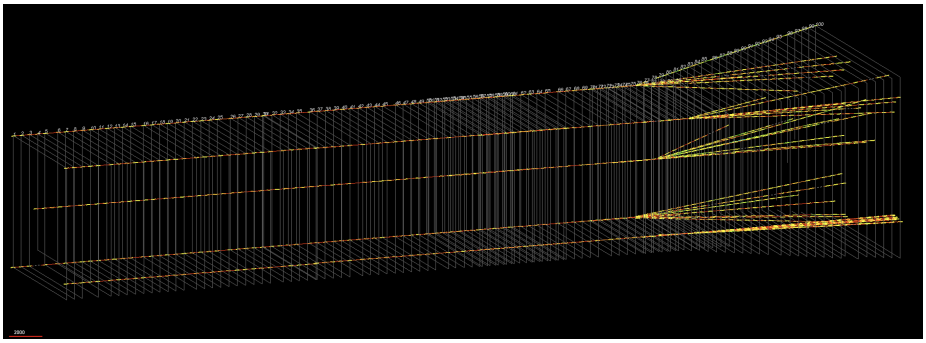


Figure 4.12: A subset of the data containing fully reconstructed proton interactions is visualized using the FEDRA [28]. The visualization shows linked primary proton tracks, associated vertices, and daughter particles. For clarity, only a few of the tracks are selected and displayed.

In Figure 4.12, the final result of the reconstruction process is visualized. The module-wide proton trajectories are traced using the proton linking method, and interaction vertices are reconstructed through the vertex reconstruction algorithm. Afterward, secondary particles are attached to the parent track and its corresponding vertex.

4.1.7 Data Quality Check

The data quality for each module and sub-area is not consistently optimal, as numerous factors can influence it. For instance, poor beam quality during irradiation or human errors in labor-intensive tasks such as emulsion film development can negatively affect data quality. Additionally, inefficiencies in the reconstruction process can further contribute to poor data quality. As illustrated in Figure 4.13, various modules were evaluated for the spatial distribution of vertices. The homogeneous distribution observed in module PD05 indicates high data quality, whereas the less dense regions in module PD06 indicate the presence of missing sub-areas within the module. The quality of all modules from the pilot run were examined, and the module named PD05 was selected for further analysis.

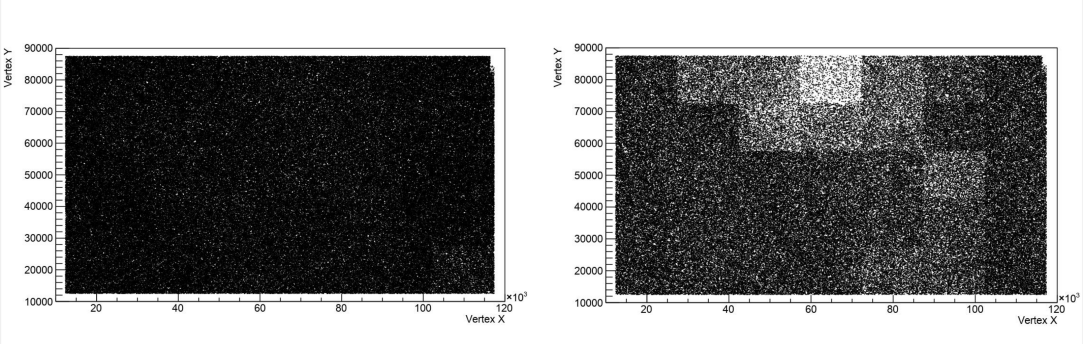


Figure 4.13: Comparison of the spatial distribution of vertices along the transverse axis: the left panel displays module PD05, while the right panel shows module PD06.

During the vertexing process, the border sub-areas of the module were excluded due to their low efficiencies. An additional study was conducted to better understand the relationship between efficiency and sub-areas, revealing that the module's bottom two rows exhibited lower efficiencies than the others. Consequently, these low-efficiency sub-areas were also removed. As a result, only 21 high-quality sub-areas remained

out of the original 63 (Figure 4.14).

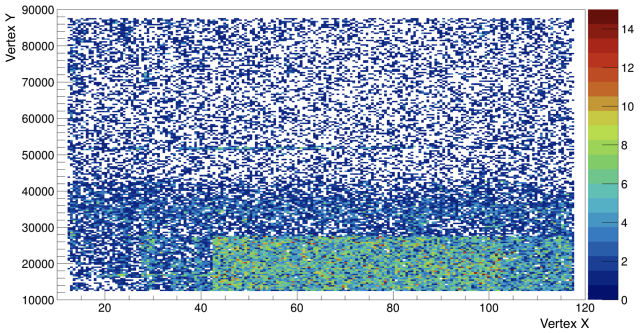


Figure 4.14: Spatial distribution of vertices that do not match with proton links in transverse axis. Dense areas below 40000 indicates low efficiency sub-areas.

Further analysis of low-quality areas revealed that the beam angle distribution within these sub-areas is asymmetric, and their standard deviation exceeds the average beam angle (Figure 4.15). This asymmetry leads to a greater number of tracks exiting the sub-areas, resulting in reduced efficiencies.

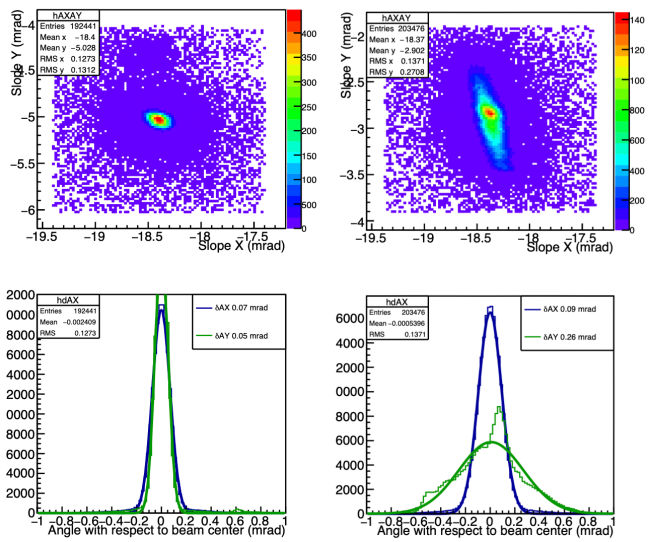


Figure 4.15: Data quality histograms for high-quality sub-area (left), and low-quality sub-area (right).

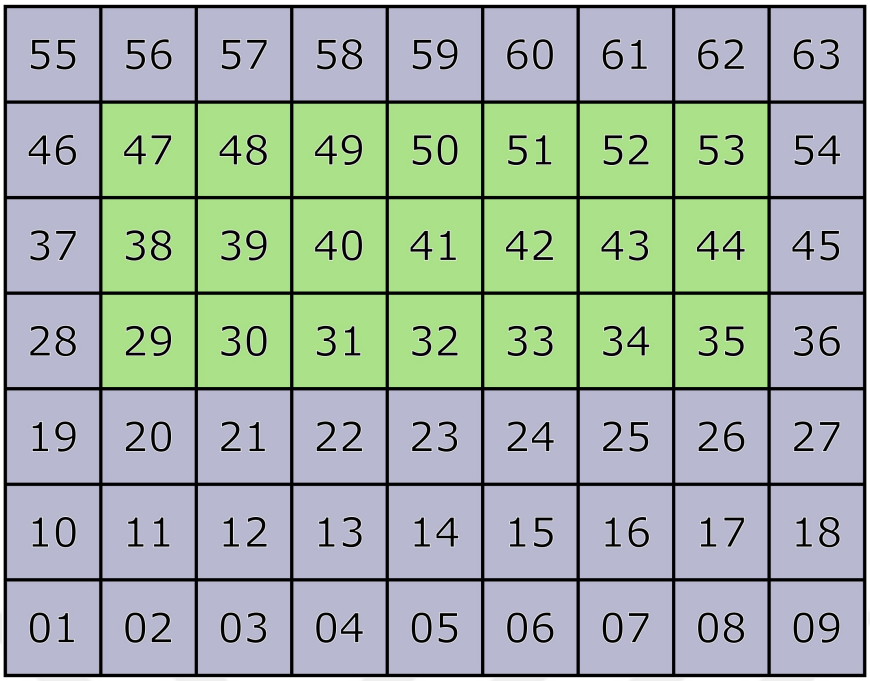


Figure 4.16: Selected 21 high-quality sub-areas is depicted in green.

As a result, 21 high-quality sub-areas are selected for data analysis, corresponding to a total surface area of 47.25 cm^2 4.16.

4.2 Monte Carlo Simulation

Monte Carlo (MC) event generation was performed using several widely used MC generators to compare the data results with event generators predictions and estimate the efficiency of the reconstruction process. These generators include GEANT4 [23], PYTHIA8 [25], EPOS [24], QGSJET [26], and DPMJET [27]. These five MC generators were employed only for event-generation purposes. The generated events were then processed through the primary MC generator, GEANT4, and supplemented with non-interacting protons to match the proton count in the data. 10% of the protons are expected to interact with all tungstens throughout the entire module. Consequently, ten times more protons were added to the externally generated primary proton events to achieve this number.

Upon completion of the Monte Carlo generation, the exact reconstruction procedure applied to the experimental data is also applied to the MC-generated data. The reconstruction process ensures that the data structure is consistent between the experimental and MC data. The effects of inefficiencies arising from the reconstruction process can be measured by comparing the true MC data with the reconstructed MC data.

4.3 Efficiency Estimation

Each stage of the reconstruction process introduces an additional inefficiency to the final reconstructed data. It is essential to quantify this inefficiency and adjust the number of interactions and related parameters accordingly to ensure accurate measurements.

The efficiency calculation is performed using EPOS Monte Carlo (MC) simulation. This involves comparing the MC outputs before the reconstruction process (True MC) with those obtained after the reconstruction process (Reconstructed MC). First, the distribution of the distances between each vertex in the reconstructed and true MC is plotted into histograms along three axes, referred to as ΔX, ΔY, and ΔZ distributions (Figure 4.17). While the ΔX and ΔY distributions show similar patterns, the ΔZ distribution shows a larger standard deviation. A Gaussian fit is applied to these

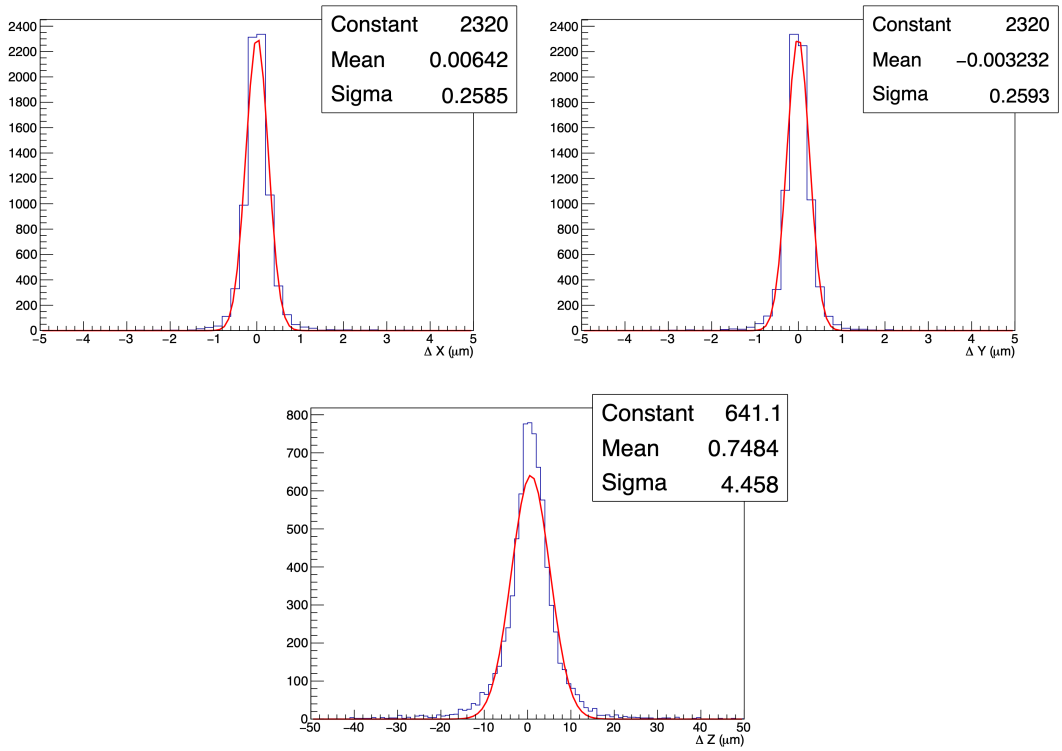


Figure 4.17: Distance between true and reconstructed vertex position in X, Y, and Z axes.

distributions, and a vertex is considered as correctly reconstructed if it falls within the 4-sigma region. Additionally, the number of matched vertices is counted to check for double-matching vertices, revealing only one matching vertex within the 4-sigma selection.

4.3.1 Selection of Minimum Ionizing Particles

Relativistic particles dissipate their energy within a medium through ionization or atomic excitation [7]. For a particle traversing a medium, a specific energy exists at which minimum ionization occurs. As demonstrated in the stopping power versus $\beta\gamma$ distribution for μ^+ in a copper medium 4.18, this minimum ionization is associated with a certain velocity.

Ionization occurs when incoming particles interact with the atoms of the medium. The degree of ionization depends on the particle's energy and the characteristics of

the medium.

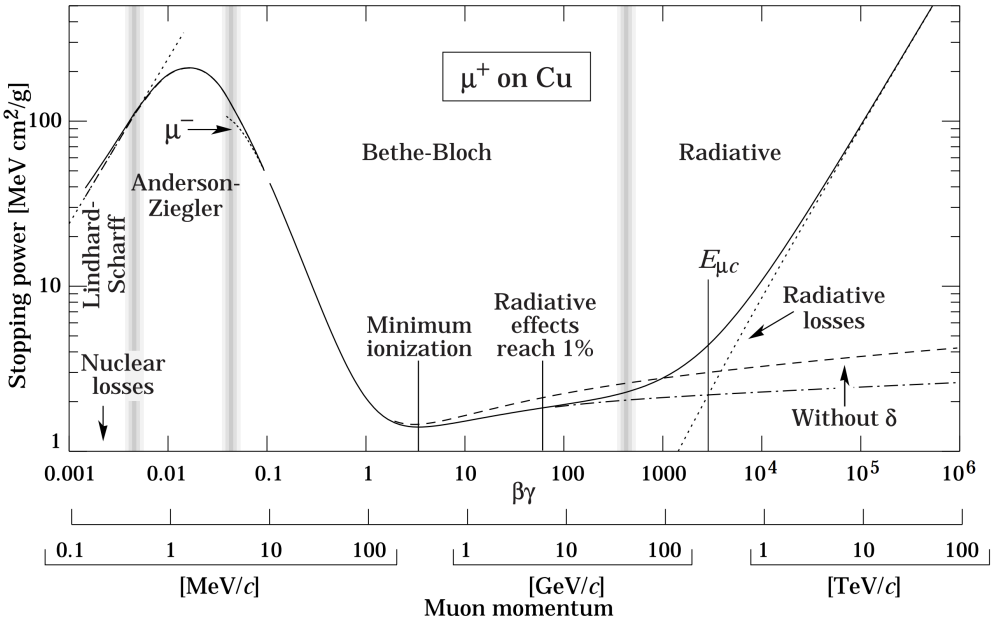


Figure 4.18: Bethe-Bloch curve for μ in copper medium.

As observed in the Bethe-Bloch curve (Figure 4.18), the region preceding minimum ionization decreases with $1/v^2$ (where v represents particle velocity), while it increases beyond the minimum ionization point. This phenomenon occurs because particles with lower momentum have more time to interact with the medium, increasing interactions. However, after the minimum ionization point, the β factor becomes dominant, leading to greater energy loss per interaction and increased stopping power.

Particles near the minimum ionization point are called minimum ionizing particles (MIPs).

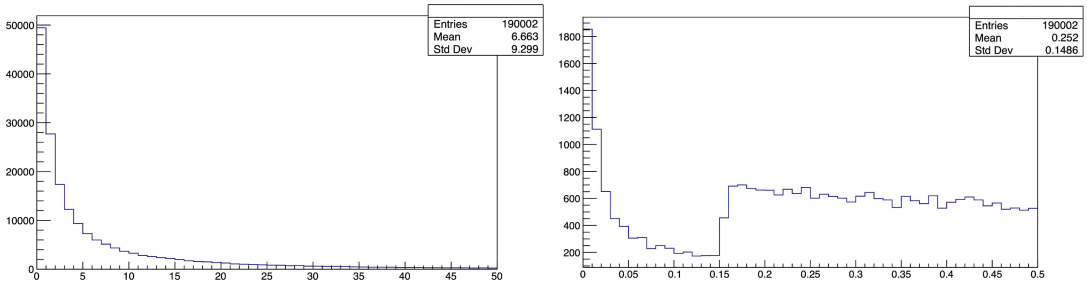


Figure 4.19: $\beta * Momentum$ histograms full view (left), zoomed (right) into 0-0.50 GeV/c region.

As illustrated in the $\beta * Momentum$ histogram Figure 4.19, the MIP point is around 0.20 GeV/c. Therefore, to select MIPs from the true MC, the region where $\beta * Momentum$ < 0.30 GeV/c is excluded.

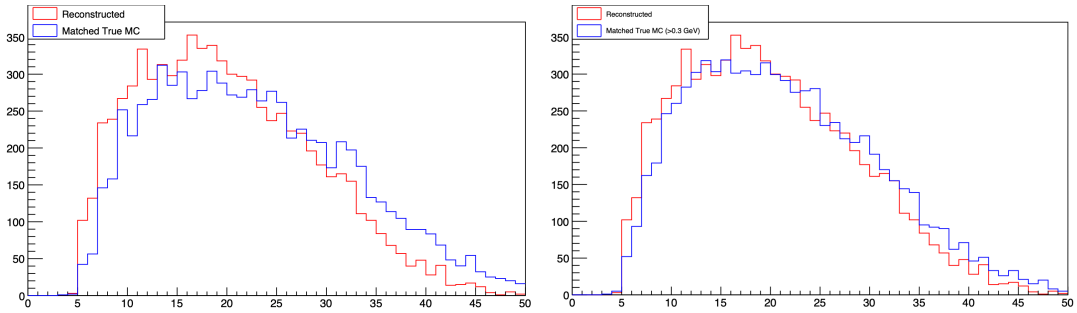


Figure 4.20: Multiplicity comparison between reconstructed and true MC before (left), and after $\beta * Momentum$ > 0.30 GeV/c cut (right).

More consistent distributions are achieved, as shown in the multiplicity comparison before and after applying the $\beta * Momentum$ > 0.30 GeV/c cut Figure 4.20. Furthermore, as depicted in Figure 4.21, MIPs mostly consist of hadrons.

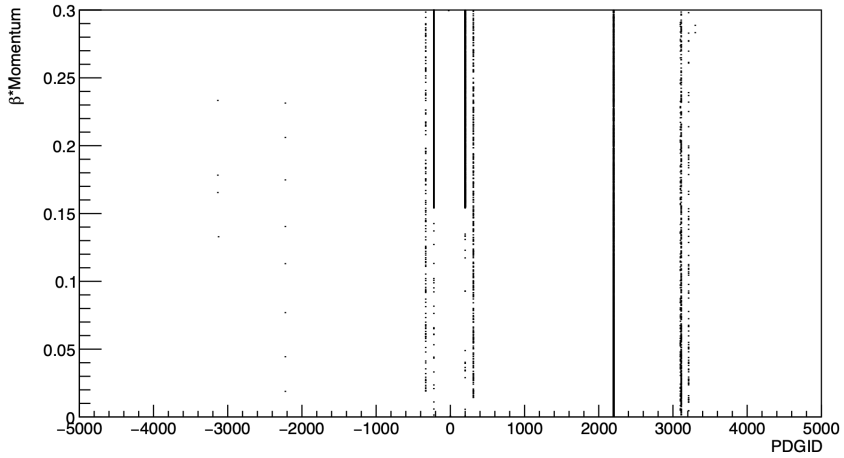


Figure 4.21: $\beta * Momentum$ < 0.30 GeV/c vs PDGID distribution.

4.3.2 Vertex Reconstruction Efficiency (ε_{vtx})

Vertex reconstruction efficiency is determined by matching true vertices with reconstructed vertices. The ratio of the number of matched vertices to the number of true vertices yields the vertex reconstruction efficiency, expressed as:

$$\text{Vertex Reconstruction Efficiency} = \frac{\text{Number of Matched Vertices}}{\text{Number of True Vertices}} \tag{4.2}$$

The Table 4.1 illustrates that vertex reconstruction efficiency is reduced in the downstream direction. This decrease is attributed to the higher density in the downstream region, where vertices are more closely spaced, thereby reducing vertex reconstruction efficiency. The mean vertex reconstruction efficiency without acceptance cut is measured to be 80.0±0.9% (Table 4.1).

Table 4.1: Vertex reconstruction efficiency for each tungsten plate.

Tungsten	**Vertex Reconstruction Efficiency (%)**
1	81.1 ± 2.5
2	80.5 ± 2.5
3	79.9 ± 2.5
4	80.2 ± 2.5
5	79.3 ± 2.5
6	79.7 ± 2.5
7	78.4 ± 2.5
8	77.2 ± 2.5
Mean	79.5 ± 0.9

The systematic error due to hadronization modeling in EPOS is estimated as 2.5% by comparing vertices with multiplicity less than five across EPOS, DPMJET, and Pythia.

4.3.3 Proton Linking Efficiency (ε_{plink})

The ratio of the number of selected protons to the number of true protons determines proton linking efficiency, expressed as:

$$\text{Proton Linking Efficiency} = \frac{\text{Number of Selected Protons}}{\text{Number of True Protons}} \tag{4.3}$$

The number of selected protons is obtained from proton-linking files, and this value is compared to the number of protons in the True MC to calculate the proton-linking efficiency. In contrast to vertex reconstruction efficiency, proton linking efficiency remains constant across the module, as track density does not influence the proton linking method. The mean proton linking efficiency without acceptance cut is measured to be 92.5±0.1% (Table 4.2).

Table 4.2: Proton linking efficiency for each tungsten plate.

Tungsten	**Proton Linking Efficiency (%)**
1	93.1 ± 0.4
2	93.3 ± 0.4
3	93.3 ± 0.4
4	93.3 ± 0.4
5	93.0 ± 0.4
6	92.5 ± 0.4
7	91.9 ± 0.4
8	91.2 ± 0.4
Mean	92.7 ± 0.1

4.3.4 Matching Efficiency (ε_{match})

Data to ROOT conversion requires proton links to be matched with the vertexing files using parent TrackIDs. However, this matching process is not entirely efficient. Interactions with a very small kink may sometimes be improperly reconstructed, resulting in one of the daughter tracks being directly connected to the parent track. Consequently, in the final analysis, a particle appears to interact and decay into new particles at the vertex while continuing to move in the same direction as the original particle. This phenomenon is referred to as mis-reconstruction. The rate of mis-reconstruction is sensitive to track density, increasing as one moves downstream in the module.

Mis-reconstructed vertices can be matched multiple times during the data to ROOT conversion process, leading to inefficiencies in matching, known as matching efficiency. As the rate of mis-reconstruction increases, the matching efficiency decreases downstream. Direct measurement of this inefficiency is not possible; however, it can be obtained using known efficiencies by applying equation 4.6. The mean matching efficiency without acceptance cut is calculated as 96.1±0.1% (Table 4.3).

Table 4.3: Matching efficiency for each tungsten plate.

Tungsten	**Matching Efficiency (%)**
1	94.2 ± 0.1
2	93.6 ± 0.1
3	92.7 ± 0.1
4	91.9 ± 0.1
5	90.2 ± 0.1
6	88.8 ± 0.1
7	88.5 ± 0.1
8	87.1 ± 0.1
Mean	90.9 ± 0.1

4.3.5 Acceptance Efficiency (ε_{acc})

To account for the migration of reconstructed vertices into emulsion or tungsten, an acceptance cut is applied along the z-axis. The ΔZ distribution indicates that the maximum distance a vertex can be reconstructed from its true position is 18 micrometers. Therefore, by excluding 18 micrometers from both ends of the module (Figure 4.22), we can effectively prevent vertices from migrating into a different medium.

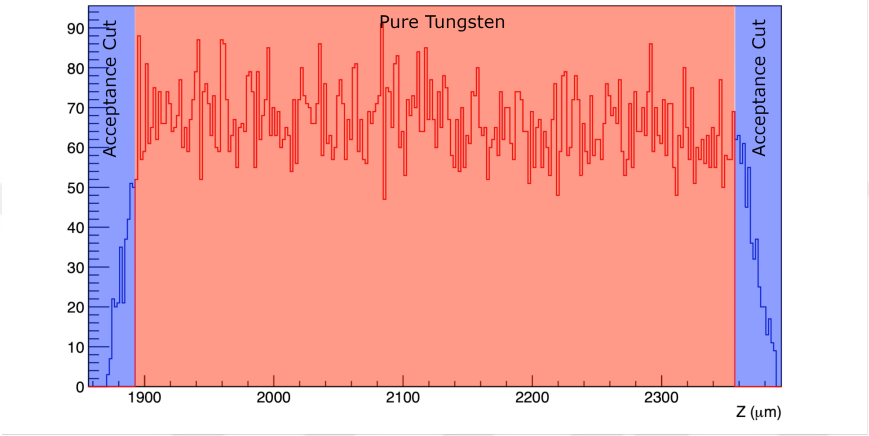


Figure 4.22: The z-axis distribution of vertex positions within the tungsten plate, including an acceptance cut of 18 microns, is shown.

The implementation of the acceptance cut introduces a new metric known as acceptance efficiency. Acceptance efficiency is calculated by taking the ratio of the vertex reconstruction efficiency before the acceptance cut to the vertex reconstruction efficiency after the acceptance cut, expressed as:

$$\text{Acceptance Efficiency} = \frac{\text{Number of Reconstructed Vertices within Acceptance}}{\text{Number of Vertices in the Tungsten Plate}} \tag{4.4}$$

The mean acceptance efficiency has been measured to be $92.8 \pm 0.1\%$ and it is constant for each tungsten plate.

Reconstruction efficiencies are corrected with the acceptance efficiency to estimate efficiencies within the acceptance. Reconstruction efficiencies with acceptance cut is shown in the Table 4.4.

Table 4.4: Vertex reconstruction efficiency for each tungsten plate with acceptance cut.

Tungsten	Vertex Reconstruction Efficiency (%)
1	75.7 ± 2.5
2	76.1 ± 2.5
3	74.5 ± 2.5
4	75.2 ± 2.5
5	74.0 ± 2.5
6	74.2 ± 2.5
7	73.7 ± 2.5
8	72.4 ± 2.5
Mean	74.5 ± 0.9

4.3.6 Total Efficiency (ε_{tot})

The total efficiency is derived by multiplying all the previously introduced efficiencies, represented as:

$$\varepsilon_{\text{tot}} = \varepsilon_{\text{vtx}} \times \varepsilon_{\text{plink}} \times \varepsilon_{\text{match}} \times \varepsilon_{\text{acc}} \tag{4.5}$$

This total efficiency directly impacts the primary proton interaction. The number of proton interactions can be accurately corrected by applying the total efficiency. Additionally, the mean total efficiency can be calculated using the ratio of the number of matched primary vertices to the number of true primary vertices, expressed as:

$$\text{Total efficiency} = \frac{\text{Number of Matched Primary Vertices}}{\text{Number of True Primary Vertices}} \tag{4.6}$$

The mean total efficiency without acceptance cut is determined to be $71.0 \pm 0.8\%$ (Table 4.5).

Table 4.5: Total efficiency for each tungsten plate.

Tungsten	Total Efficiency
1	71.7 ± 2.3
2	71.5 ± 2.3
3	69.4 ± 2.3
4	69.1 ± 2.3
5	66.9 ± 2.3
6	65.6 ± 2.3
7	64.6 ± 2.3
8	62.0 ± 2.3
Mean	67.6 ± 0.8

4.3.7 Data-Driven Efficiencies

The efficiency of Monte Carlo (MC) must be utilized to correct data-related parameters. However, as illustrated in the figure 4.23, the track density in the data differs from that in the MC simulations. Therefore, track density-dependent efficiencies cannot be directly applied to the data.

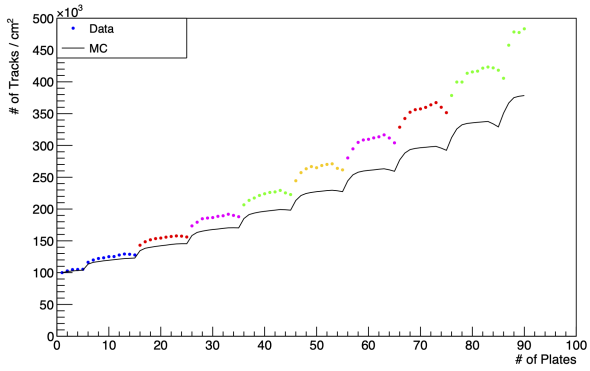


Figure 4.23: The distribution of track density for both Monte Carlo simulations and experimental data is illustrated, with dots indicating the data and solid line is representing the EPOS result.

Efficiency versus track density plots are generated for each tungsten plate to estimate

the efficiency of the data. These plots reveal that efficiencies have a linear dependence on track density. By performing a linear fit to the data points, a track density-dependent linear function can be derived for each reconstruction efficiency (Figure 4.24).

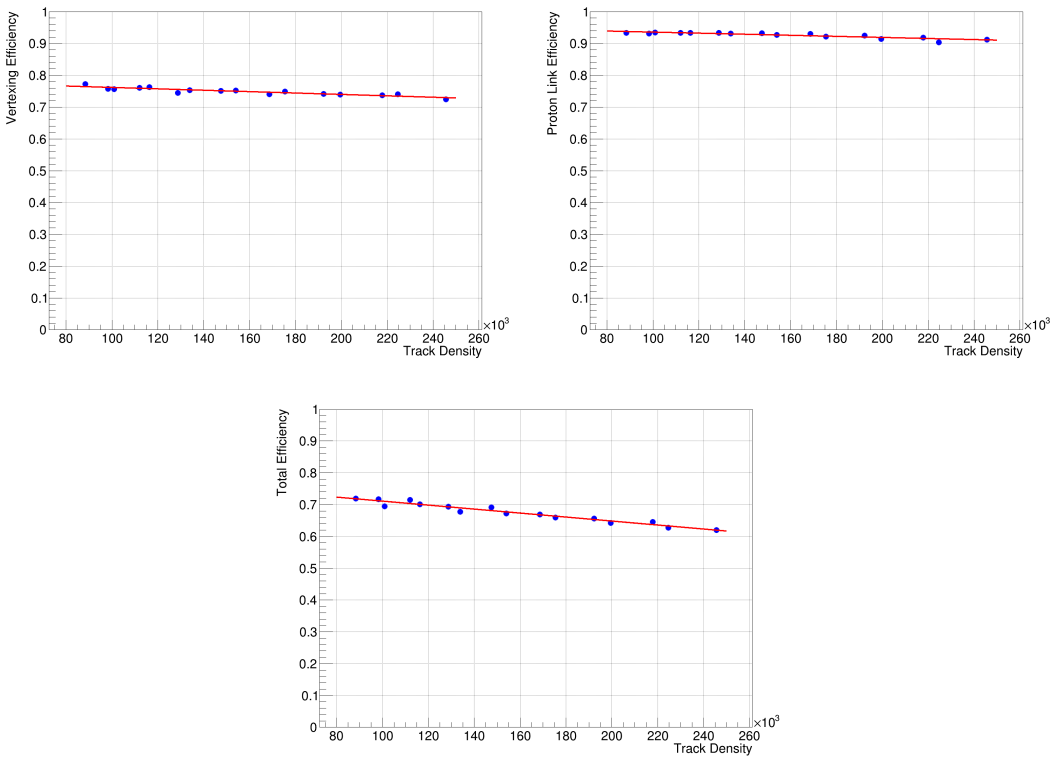


Figure 4.24: A scatter plot illustrating the relationship between MC efficiencies and track density is presented, along with a linear fit. The plots include efficiencies for vertex reconstruction, proton linkage, and total efficiency.

$$\varepsilon_{vtx} = -2.20 \times 10^{-7}\rho + 0.783 \tag{4.7}$$

$$\varepsilon_{plink} = -1.67 \times 10^{-7}\rho + 0.952 \tag{4.8}$$

$$\varepsilon_{tot} = -6.27 \times 10^{-7}\rho + 0.773 \tag{4.9}$$

where ρ is the track density.

Since the track density in the data is known, a data-driven efficiency can be estimated for empirical data using these linear functions (Figures 4.7 - 4.8 - 4.9). Estimated data-driven efficiencies are shown in the table 4.6.

Table 4.6: Table of estimated data-driven efficiency through track density using linear functions.

Tungsten	$\rho\ (tracks/cm^2)$	$\varepsilon_{vtx}\ (\%)$	$\varepsilon_{plink}\ (\%)$	$\varepsilon_{tot}\ (\%)$
1	86,291	76.4 $\pm$ 2.5	93.8 $\pm$ 0.4	71.9 $\pm$ 2.3
2	104,756	76.0 $\pm$ 2.5	93.5 $\pm$ 0.4	70.7 $\pm$ 2.3
3	127,921	75.5 $\pm$ 2.5	93.1 $\pm$ 0.4	69.3 $\pm$ 2.3
4	154,027	74.9 $\pm$ 2.5	92.6 $\pm$ 0.4	67.6 $\pm$ 2.3
5	182,588	74.3 $\pm$ 2.5	92.2 $\pm$ 0.4	65.9 $\pm$ 2.3
6	214,386	73.6 $\pm$ 2.5	91.6 $\pm$ 0.4	63.9 $\pm$ 2.3
7	249,238	72.8 $\pm$ 2.5	91.0 $\pm$ 0.4	61.7 $\pm$ 2.3
8	288,145	72.0 $\pm$ 2.5	90.4 $\pm$ 0.4	59.2 $\pm$ 2.3
Mean	175,919	74.4 $\pm$ 0.9	92.3 $\pm$ 0.1	66.3 $\pm$ 0.8

4.3.8 Proton Purity

Proton purity quantifies the accuracy of correctly selecting protons using the proton selection method within the first sub-volume. It indicates the proton selection process's effectiveness. Proton purity is calculated by the ratio of the number of correctly selected protons to the total number of selected particles, expressed as:

$$\text{Proton Purity} = \frac{\text{Number of Correctly Selected Protons}}{\text{Number of All Selected Particles}} \tag{4.10}$$

The mean proton purity has been measured to be $96.7 \pm 0.1\%$.

4.3.9 Multiplicity Dependence of Vertex Reconstruction Efficiency

The vertex reconstruction efficiency as a function of the multiplicity of charged tracks is illustrated in the figure. Notably, no reconstructed events with a multiplicity of less than 5 represent a general threshold for vertex reconstruction. For multiplicities greater than 5, the vertex reconstruction efficiency increases, reaching a plateau of > 95% efficiency after multiplicity of 12 as shown in figure 4.25.

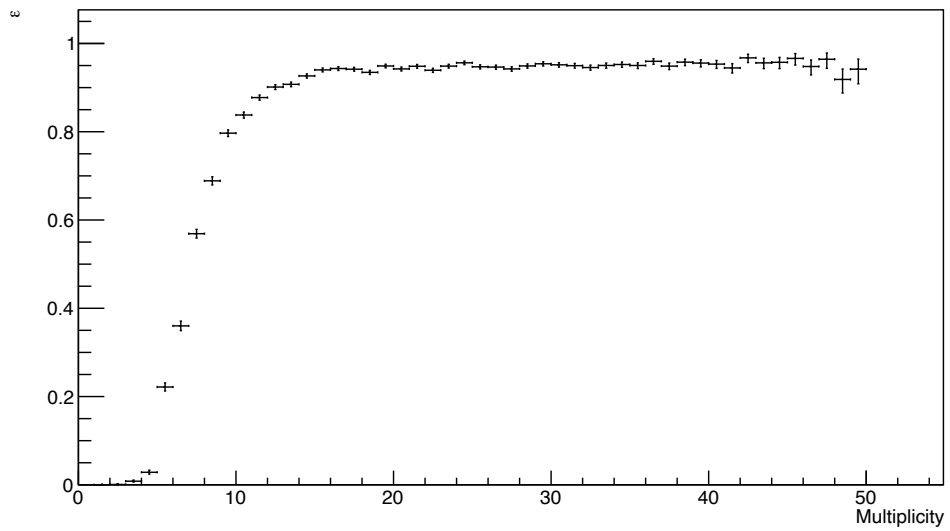


Figure 4.25: The efficiency of vertex reconstruction is analyzed as a function of the multiplicity of charged tracks at the vertex.

CHAPTER 5

FIRST RESULTS FROM PILOT RUN

5.1 Proton Interaction Rate

The proton interaction rate is defined as the ratio of primary protons interacting with the target to the number of beam protons. This interaction rate is influenced by factors such as the target material, target thickness, and the energy of the primary protons.

To validate the data measurements, the proton interaction rate in the experimental data can be compared with that obtained from MC simulations. The DsTau experiment was replicated in the MC simulations using identical parameters. The thickness of the tungsten plate is fixed to 464 microns for both data and MC simulation 4.22.

The difference in the refractive index between the emulsion and the plastic base requires an adjustment of the measured slopes by a correction factor of 1.052 ± 0.002 [20]. After this adjustment, the effective thickness of the tungsten plate in data is determined to be 489 ± 1 μm. Since the interaction rate is sensitive to tungsten thickness, comparing the proton interaction rate density is more appropriate.

The table 5.1 shows that the interaction rate remains constant after efficiency corrections, demonstrating that the interaction rate is independent of the number of incident protons because fewer primary protons are expected downstream due to interactions in the preceding material. Furthermore, the consistency between the MC and data measurements of the proton interaction rate density confirms the validity of the empirical data measurements.

In conclusion, the mean proton interaction rate density per millimeter of tungsten is measured to be 1.08 ± 0.01 $\%/mm$ in the data and 1.06 ± 0.01 $\%/mm$ in the MC.

Table 5.1: The proton interaction rate per unit length in the tungsten is estimated for data and EPOS.

Tungsten	**Data** ($\%/mm$)	**EPOS** ($\%/mm$)
1	1.10 ± 0.01	1.06 ± 0.01
2	1.10 ± 0.01	1.06 ± 0.01
3	1.07 ± 0.01	1.06 ± 0.01
4	1.07 ± 0.01	1.06 ± 0.01
5	1.07 ± 0.01	1.07 ± 0.01
6	1.07 ± 0.01	1.08 ± 0.01
7	1.07 ± 0.01	1.05 ± 0.01
8	1.05 ± 0.01	1.06 ± 0.01
Mean	1.08 ± 0.01	1.0 ± 0.016

5.2 MC / Data Comparisons

The reconstructed MC data from five different event generators are compared [21] with data to identify the MC simulation that most accurately represents the our data.

A comparative analysis between MC and data results is conducted in terms of three parameters: impact parameter (Figure 5.1), charged track multiplicity (Figure 5.2), and track angles (Figure 5.3). As illustrated in the figures, the QGSJET provides the closest match to the data for the impact parameter distribution, while the EPOS best matches the data for both the multiplicity and track angle distributions. Consequently, the EPOS is determined to be the best event generator for representing DsTau data overall. Therefore, EPOS is employed for analysis and comparison in this work.

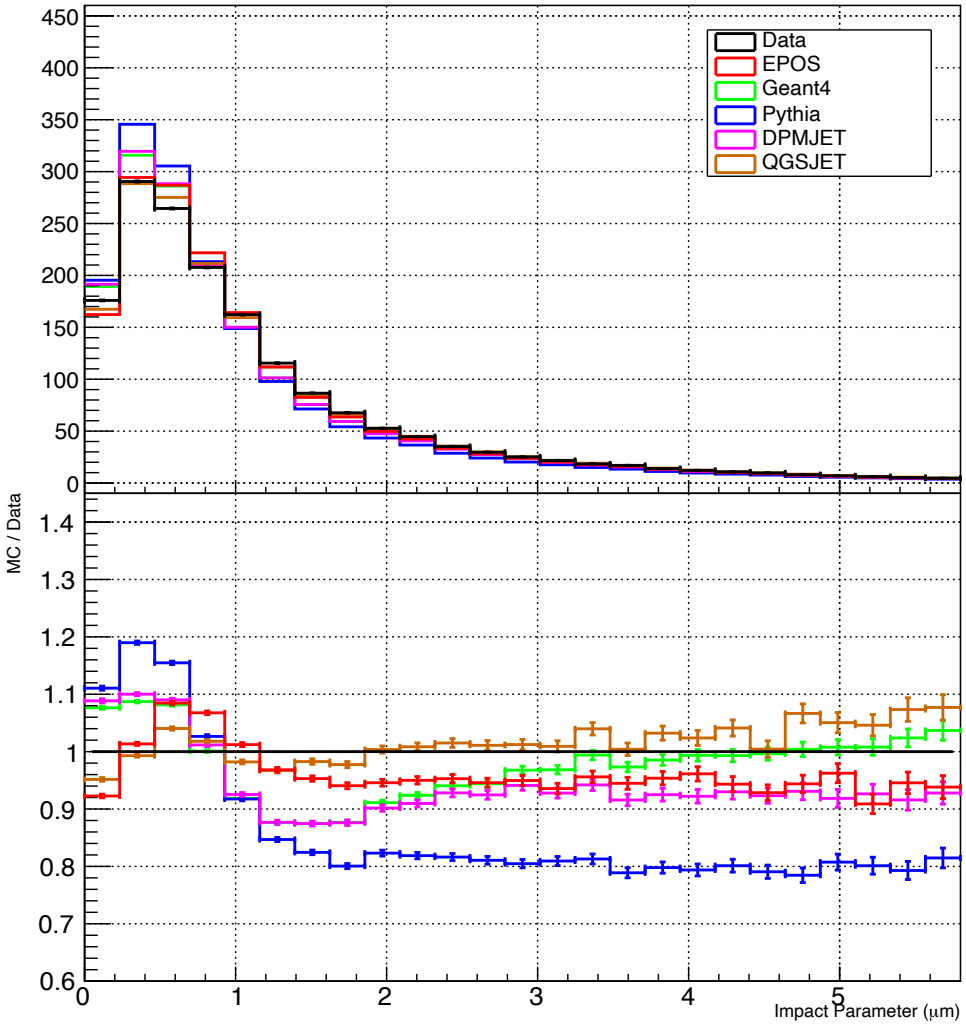


Figure 5.1: A comparison between MC simulations and experimental data for impact parameter is shown, MC is normalized to the number of tracks in the data. The lower section of the histogram illustrates the ratio of MC to data. The constant black line represents the data.

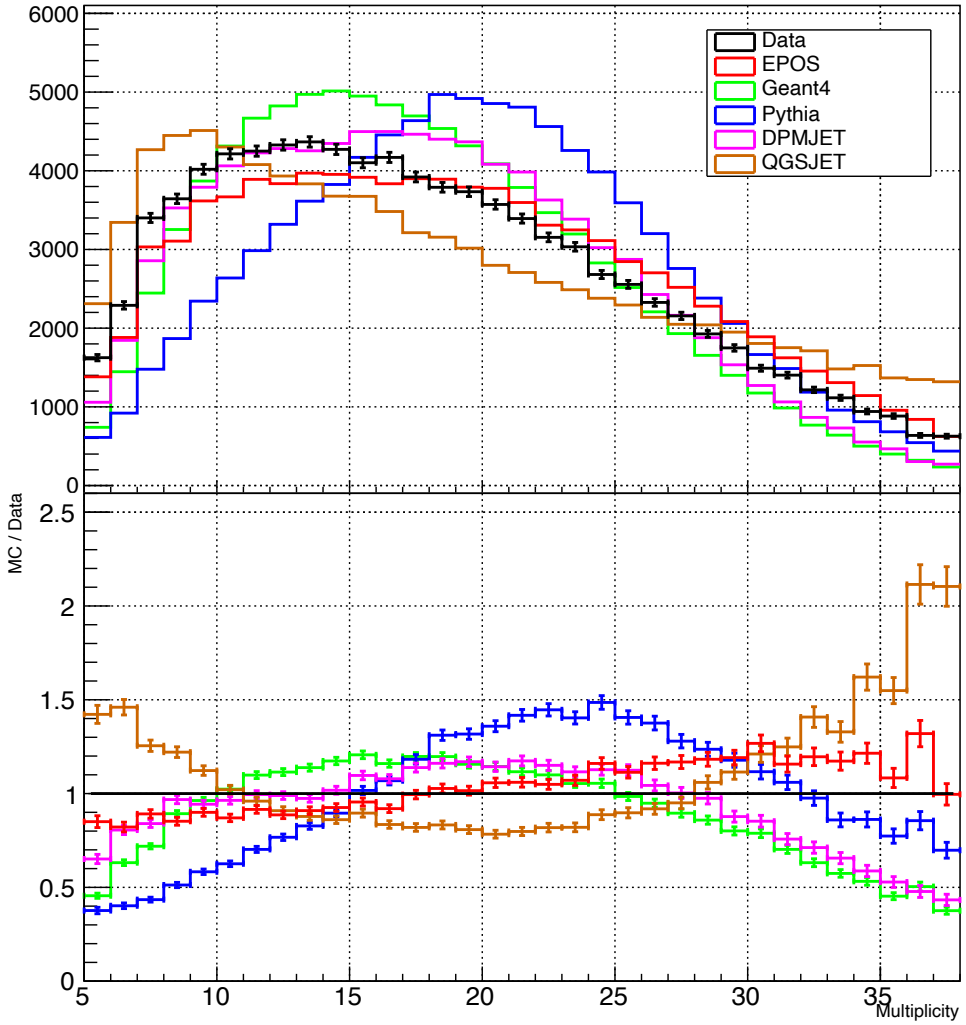


Figure 5.2: A comparison between MC simulations and experimental data for track multiplicity is shown, MC is normalized to the number of events in the data. The lower section of the histogram illustrates the ratio of MC to data. The constant black line represents the data.

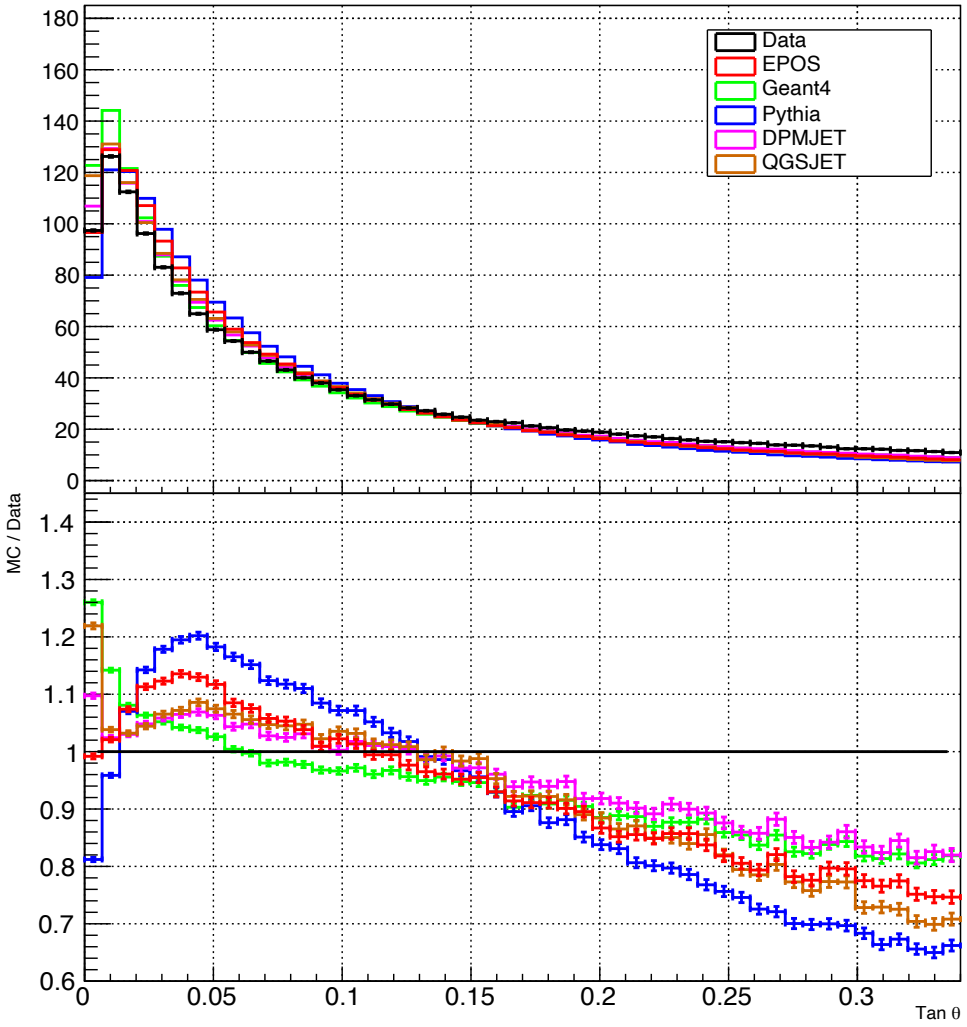


Figure 5.3: A comparison between MC simulations and experimental data for track angle is shown, MC is normalized to the number of tracks in the data. The lower section of the histogram illustrates the ratio of MC to data. The constant black line represents the data.

However, a notable difference in the track angle distribution for ($\tan(\theta)$) greater than 0.05 is apparent. The discrepancy at larger angles is further analyzed to understand the underlying reason. Figure (5.4) illustrating the particle slope angle versus multiplicity distribution in the data and MC simulations (EPOS and QGSJET) reveal that the data and EPOS show similar distributions, with track angles increasing as multiplicity increases. This phenomenon can be explained by the constant transverse momentum (P_t) distribution of hadron interactions in the MC generators [22]. The average transverse momentum distribution of the hadronization process simulated in the MCs remains constant. Also, the QGSJET results show a clear discrepancy compared to the data and EPOS.

To further investigate, the track angle distribution is analyzed in two different multiplicity regions: less than ten (Figure 5.5) and greater than or equal ten (Figure 5.6). The Figures show that the multiplicity region with fewer than ten tracks demonstrates good agreement between the MC simulations and the data. However, a noticeable discrepancy is evident in the region with a multiplicity greater than or equal ten.

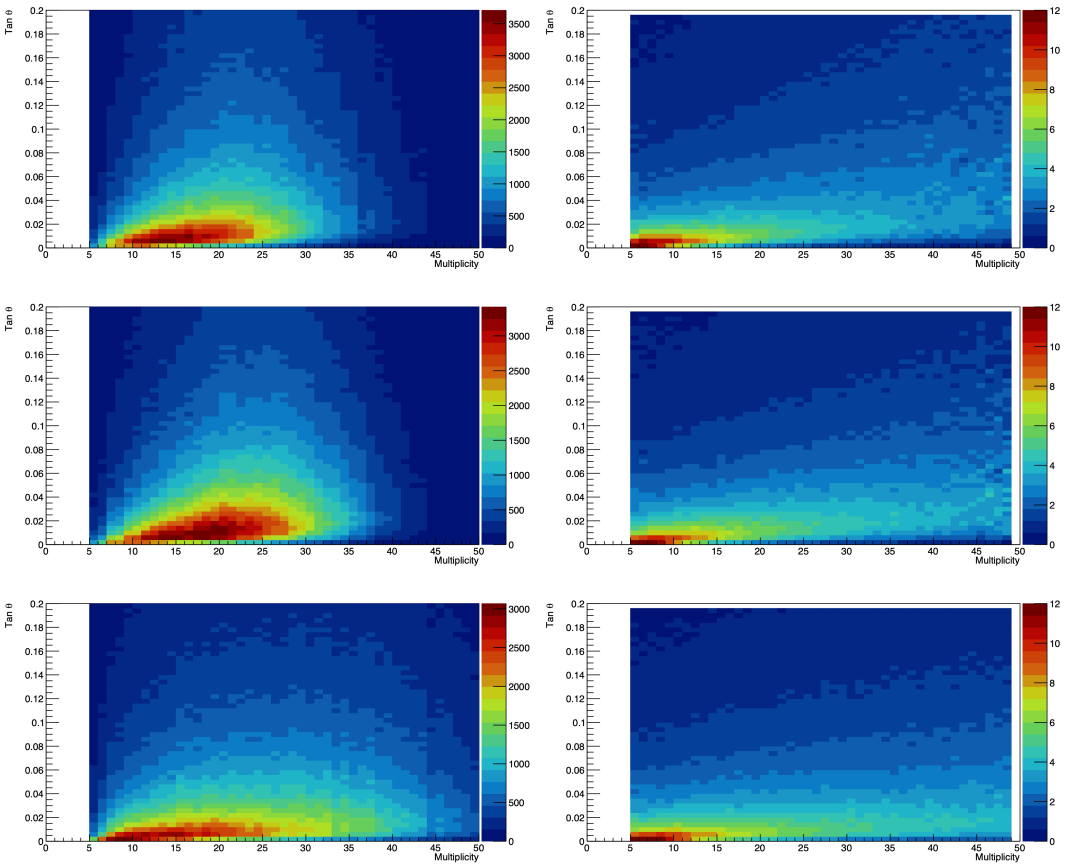


Figure 5.4: The left panel displays the distribution of track slope versus multiplicity in the experimental data, EPOS and QGSJET respectively (from top to bottom). The right panel presents the same distribution but they are normalized to each multiplicity bin.

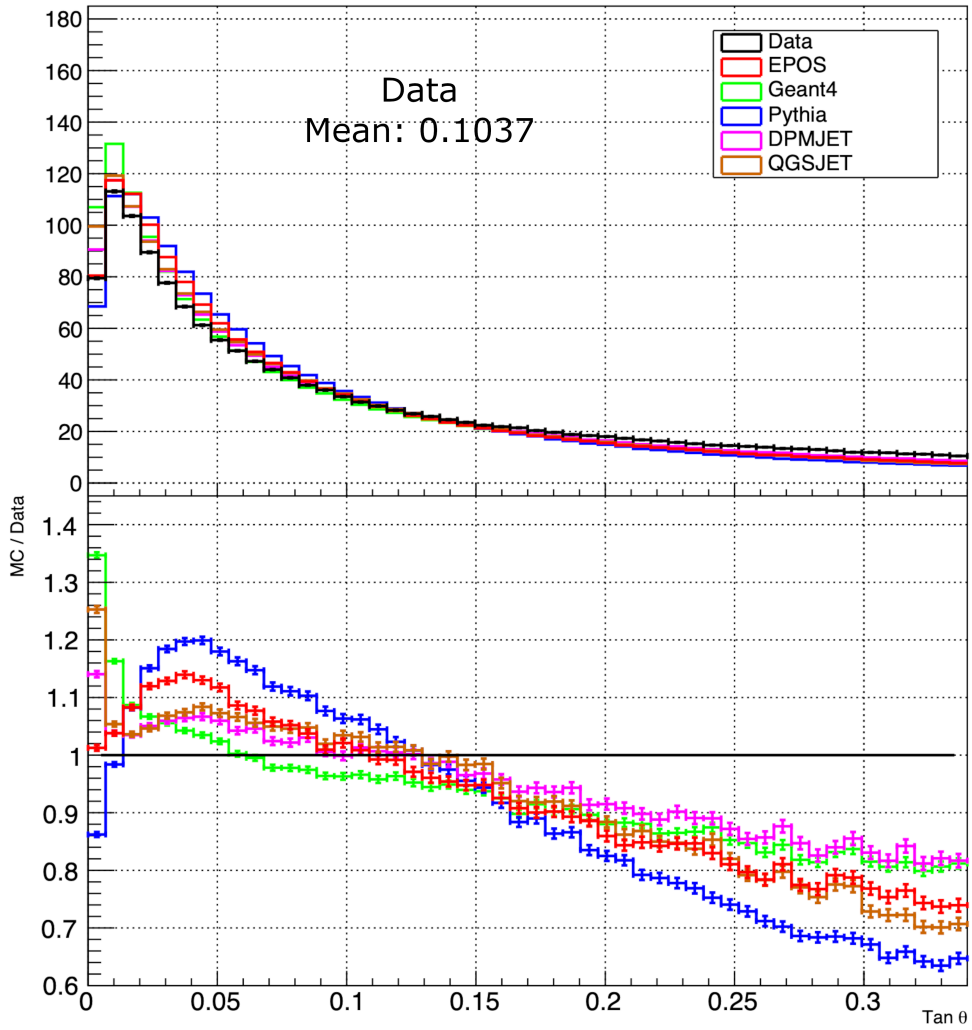


Figure 5.5: A comparison between MC simulations and experimental data for track slope less than 10 is shown, MC is normalized to the number of tracks in the data. The lower section of the histogram illustrates the ratio of MC to data. The constant black line represents the data.

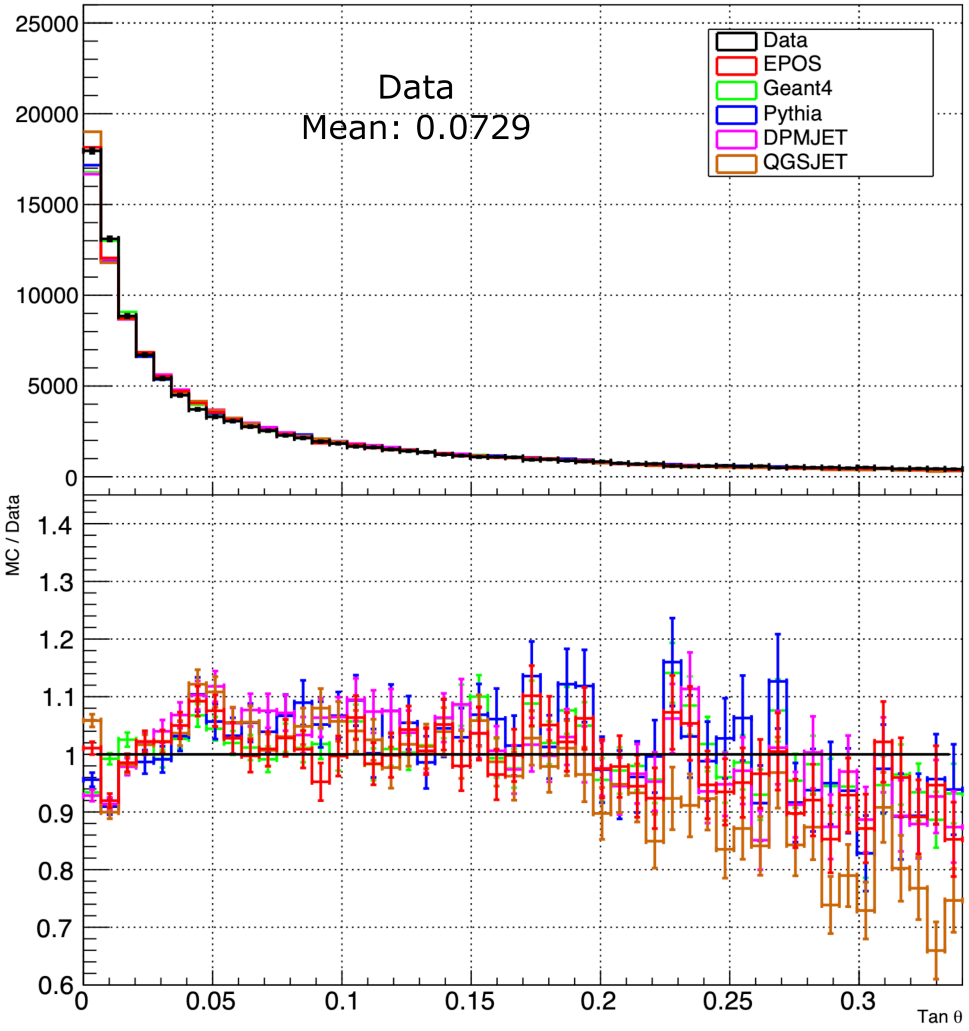


Figure 5.6: A comparison between MC simulations and experimental data for track slope greater than or equal to 10 is shown, MC is normalized to the number of tracks in the data. The lower section of the histogram illustrates the ratio of MC to data. The constant black line represents the data.

5.3 KNO-G Scaling

KNO scaling was introduced in 1972 by Z. Koba, H.B. Nielsen, and P. Olesen [29]. The idea behind KNO scaling is to find a universal function that describes the probability distribution of particle multiplicities in high-energy collisions independent of the center-of-mass energy of the collision. However, this function was not satisfactory for all energy levels. Later, A.I. Golokhvastov [30] reformulated the scaling function to ensure its applicability across the entire energy spectrum, referred to as KNO-G scaling.

5.3.1 Formulation of KNO-G Scaling

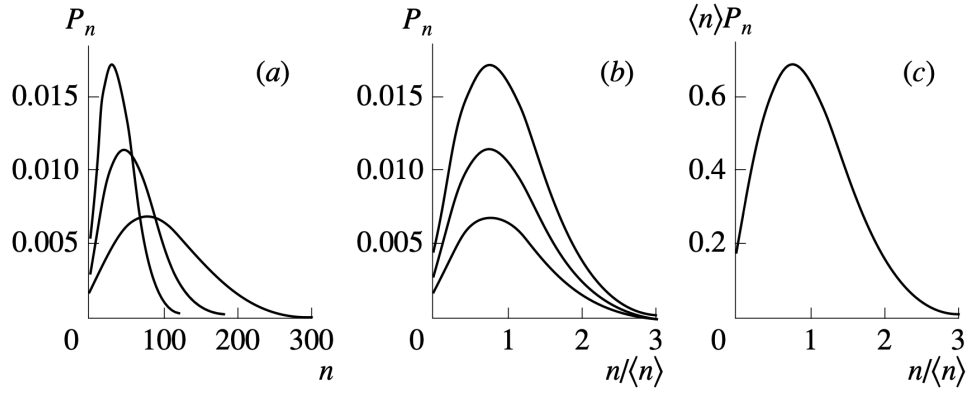


Figure 5.7: (a) Multiplicity distribution with different center-of-mass energies. (b) Multiplicity axis normalized is normalized with mean multiplicity. (c) Probability axis is scaled with mean multiplicity so they coincide at each point.

Figure 5.7 a illustrates the probability distribution of multiplicities at high beam energies. As the figure shows, different beam energies result in varying multiplicity distributions. With increasing beam energy, the mean of the multiplicity distribution also increases. In Figure 5.7 a, the area under each curve is unity, representing the sum of all probabilities. However, in Figure 5.7 b, after normalizing with the mean multiplicity $\langle n\rangle$, the new mean values of the multiplicity distribution are the same for all energies. Despite this, the area under the curve is neither unity nor consistent across the curves. Therefore, the horizontal axis must be scaled by the mean multi-

plicity to restore the area under the curve to unity. KNO scaling states that the curves will coincide at each point after the scaling Figure 5.7 c.

KNO scaling states that:

$$\langle n \rangle P_n = \Psi \left(\frac{n}{\langle n \rangle} \right) \tag{5.1}$$

The mean multiplicity, denoted as $\langle n \rangle$, is expressed by the following relationship.

$$\langle n \rangle = \sum_n n P_n \tag{5.2}$$

Normalization conditions for the distribution can be written as:

$$\int_0^\infty \Psi\left(z\right)\, dz = 1 \tag{5.3}$$

$$\int_0^\infty \Psi\left(z\right) z\, dz = 1 \tag{5.4}$$

where, $z = \frac{n}{\langle n \rangle}$. The normalization conditions (Eqns 5.3-5.4) are satisfied for larger values of $\langle n \rangle$ (corresponding to higher energies). This is because the distribution becomes continuous at higher $\langle n \rangle$, whereas at lower $\langle n \rangle$, a discrete distribution is observed Figure 5.8. Consequently, the original KNO formulation is highly effective at asymptotic energies; however, at lower energies, the discrete nature of the distribution introduces some discrepancies. Golokhvastov formulated a new function that is applicable across all energy ranges to address this issue.

In his publication [30], Golokhvastov proposed that the following equations can describe the multiplicity distribution for proton-proton interactions:

$$\Psi_1^{pp}\left(z\right) = a_1 z^{a_3} exp\left(-a_2 z^2\right) \tag{5.5}$$

$$\Psi_2^{pp}\left(z\right) = b_1\left(z + b_3\right) exp\left[-b_2\left(z + b_3\right)\right] \tag{5.6}$$

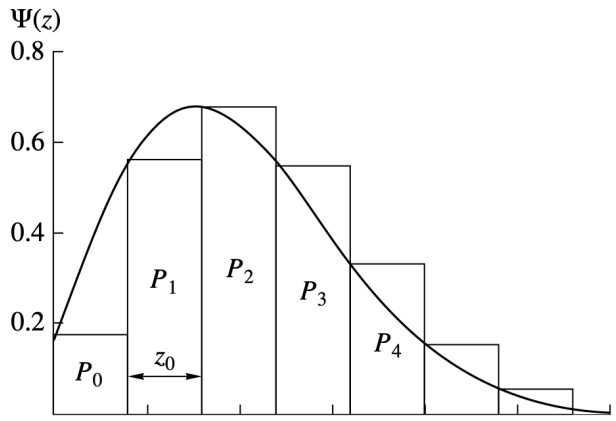


Figure 5.8: Discrete multiplicity distribution at low energies.

where the parameters are defined as a_1 = 1.19, a_2 = 0.62, a_3 = 0.66, b_1 = 1.25, b_2 = 0.62, and b_3 = 0.14. These functions represent the multiplicity distribution across all energy levels for proton-proton interactions.

5.3.2 Application of KNO-G Scaling to DsTau Multiplicity Distribution

As discussed in the efficiency chapter, the efficiency varies for different multiplicities. Therefore, the multiplicity distribution is corrected for efficiency, then the mean multiplicity ($\langle n \rangle$) is calculated. Subsequently, KNO scaling is applied to the data using corrected $\langle n \rangle$.

Both equations (5.5 - 5.6) yield similar distributions and χ^2 values; hence, for simplicity, only equation 5.5 is utilized. The fitting was performed over the 0.5 < z < 3.0 range, where the multiplicity is measured with high efficiency. A comparison of our fit parameters with those provided in Golokhvastov's paper is presented in Table 5.2.

Table 5.2: Obtained KNO-G fit parameters

Ψ	Our fit	[30]
a_1	1.15 ± 0.01	1.19
a_2	0.45 ± 0.01	0.62
a_3	0.67 ± 0.02	0.66

As illustrated in Figure 5.9, the χ^2 value of the fit is 65.1 per 32 degrees of freedom, indicating a strong agreement with the experimental data.

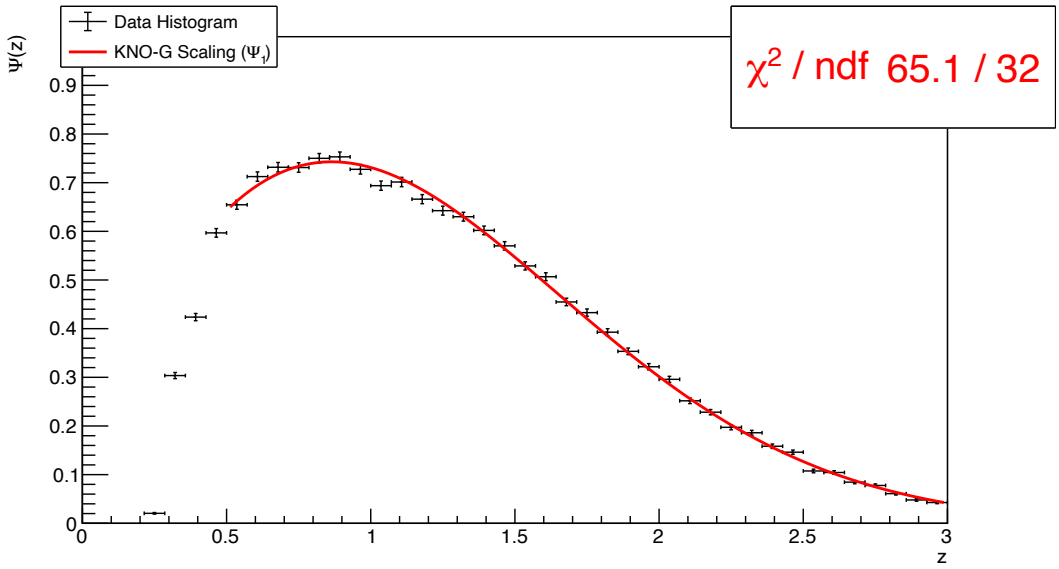


Figure 5.9: KNO-G scaling fit on DsTau multiplicity distribution.

CHAPTER 6

CONCLUSIONS

This thesis reports the first results of the DsTau experiment, including a Data/MC comparisons and the introduction of a novel reconstruction method for analyzing primary interactions.

The DsTau (NA65) experiment at CERN-SPS is dedicated to measuring the cross-section of D_s meson production, which is crucial to precisely understanding ν_τ production. The experiment successfully captures the small kink in the $D_s \rightarrow \tau$ decay topology using a nuclear emulsion-based detector with sub-micron spatial resolution.

This thesis has presented the first results from the data analysis of the 2018 run, including the development of a novel method for proton track reconstruction throughout the entire detector, so-called proton linking. With proton linking, proton tracks are selected from the beginning of the module and followed through the detector, enabling the selection of the primary proton across the module. Using proton linking, the number of primary interactions in each tungsten target was studied, and it was found that the interaction rate per unit length for each tungsten is consistent after efficiency corrections. To have a realistic efficiency estimation, track density variation in data is considered. All efficiencies are parametrized as a function of track density, and these data-driven efficiencies are used in our analysis. Comparisons with reconstructed MC results showed that data and MC results are consistent, validating the proton linking method.

A detailed analysis of the proton interaction vertex and comparisons with various MC event generator predictions were performed. Data were compared with predictions of six different event generators in track angle, multiplicity, and impact parameter.

EPOS was identified as the best representation of the DsTau data. The findings from this study hold significant potential for enhancing the accuracy of MC event generators, thereby contributing to the broader field of particle physics and improving our understanding of fundamental particle interactions.

KNO-G scaling was also tested for our data, and the fit parameters were found to be consistent with previous experiment results. This consistency demonstrates that the DsTau experiment aligns with earlier experiments regarding the charged track multiplicity.

REFERENCES

[1] Durhan, O. (2020). Searching for neutral kaons in the ship test beam data [M.S. - Master of Science]. Middle East Technical University.

[2] Cottingham, W. N., and D. A. Greenwood. An Introduction to the Standard Model of Particle Physics. 2nd ed., Cambridge University Press, 2023. DOI.org (Crossref), https://doi.org/10.1017/9781009401685.

[3] Gross, D. J., & Wilczek, F. (1973). Ultraviolet behavior of non-abelian gauge theories. Physical Review Letters, 30(26), 1343–1346. https://doi.org/10.1103/physrevlett.30.1343

[4] Semat, H. (1978). Introduction to Atomic and Nuclear Physics: 5Th edition (5th ed.). Chapman and Hall.

[5] R. Aaij *et al.* [LHCb], Nature Phys. **18** (2022) no.3, 277-282 doi:10.1038/s41567-023-02095-3 [arXiv:2103.11769 [hep-ex]].

[6] Amsler, Claude. The Quark Structure of Hadrons: An Introduction to the Phenomenology and Spectroscopy. Springer International Publishing, 2018. DOI.org (Crossref), https://doi.org/10.1007/978-3-319-98527-5.

[7] R. L. Workman *et al.* [Particle Data Group], PTEP **2022** (2022), 083C01 doi:10.1093/ptep/ptac097

[8] S. Navas *et al.* [Particle Data Group], Phys. Rev. D **110** (2024) no.3, 030001 doi:10.1103/PhysRevD.110.030001

[9] Particle Data Group, et al. “Review of Particle Physics.” Progress of Theoretical and Experimental Physics, vol. 2022, no. 8, Aug. 2022, p. 083C01. DOI.org (Crossref), https://doi.org/10.1093/ptep/ptac097.

[10] C. F. Wild, DUKHEP-87-1.

[11] N. Agafonova et al.[OPERA Collaboration], Discovery of doi:10.1103/PhysRevLett.115.121802

[12] K. Abe *et al.* [T2K], Nucl. Instrum. Meth. A **659** (2011), 106-135 doi:10.1016/j.nima.2011.06.067 [arXiv:1106.1238 [physics.ins-det]].

[13] J. Evans [MINOS], Adv. High Energy Phys. **2013** (2013), 182537 doi:10.1155/2013/182537 [arXiv:1307.0721 [hep-ex]].

[14] K. Kodama et al. [DONuT Collaboration], Observation of tau neutrino interactions, Phys.Lett.B 504 (2001) 218-224.

[15] S. Aoki et al. [DsTau Collaboration], DsTau: study of tau neutrino production with 400 GeV protons from the CERN-SPS, J. High Energ. Phys. 2020 (2020) 33.

[16] Guler, Ali Murat. "DsTau: Study of Tau Neutrino Production with Nuclear Emulsion in the CERN-SPS." SciPost Physics Proceedings, no. 8, July 2022, p. 094. DOI.org (Crossref), https://doi.org/10.21468/SciPostPhysProc.8.094.

[17] Öz, C. (2022). STUDY OF CHARMED HADRONS LIFETIME WITH 400 GEV PROTONS AT THE CERN-SPS [M.S. - Master of Science]. Middle East Technical University.

[18] Aoki, Shigeki, et al. "Development of Proton Beam Irradiation System for the NA65/DsTau Experiment." Journal of Instrumentation, vol. 18, no. 10, Oct. 2023, p. P10008. DOI.org (Crossref), https://doi.org/10.1088/1748-0221/18/10/P10008.

[19] M. Yoshimoto, T. Nakano, R. Komatani and H. Kawahara, PTEP **2017** (2017) no.10, 103H01 doi:10.1093/ptep/ptx131 [arXiv:1704.06814 [physics.ins-det]].

[20] Y. Nakamura for GRAINE Coll., PoS(KMI2017)079, Proceedings of the 3rd International Symposium on "Quest for the Origin of Particles and the Universe (2017).

[21] E. Yuksel *et al.* [DsTau], PoS **EPS-HEP2023** (2024), 144 doi:10.22323/1.449.0144

[22] O. Minakawa et al. Suppl. Nuov. Cim., vol.11(1959), pp.125–153.

[23] S. Agostinelli et.al., [GEANT4 Collaboration] GEANT4–a simulation toolkit, Nucl.Instrum.Meth.A 506 (2003) 250-303.

[24] S. Porteboeuf, T. Pierog, K. Werner, Producing Hard Processes Regarding the Complete Event: The EPOS Event Generator, https://doi.org/10.48550/arXiv.1006.2967.

[25] T. Sjöstrand et.al., An Introduction to PYTHIA 8.2, https://doi.org/10.48550/arXiv.1410.3012.

[26] S. Ostapchenko, Status of QGSJET, https://doi.org/10.48550/arXiv.0706.3784.

[27] J.Ranft, New features in DPMJET version II.5, https://doi.org/10.48550/arXiv.hep-ph/9911213.

[28] V. Tioukov et.al., The FEDRA—Framework for emulsion data reconstruction and analysis in the OPERA experiment, Nuclear Instruments and Methods in Physics Research A 559 (2006) 103–105.

[29] Z. Koba, H.B. Nielsen, P. Olesen, Scaling of multiplicity distributions in high energy hadron collisions, Nuclear Physics B, Volume 40, 1972, Pages 317-334, ISSN 0550-3213, https://doi.org/10.1016/0550-3213(72)90551-2.

[30] Golokhvastov, A.I. Koba-Nielsen-Olesen scaling. Phys. Atom. Nuclei 64, 84–97 (2001). https://doi.org/10.1134/1.1344946

[31] R. Szwed and G. Wrochna, Z. Phys. C **29** (1985), 255 doi:10.1007/BF01550826